universität wien

MASTERARBEIT / MASTER'S THESIS

Titel der Masterarbeit / Title of the Master's Thesis

„Simulating Proton Transfer in the M2 Ion Channel of the Influenza Virus A“

verfasst von / submitted by

Nóra Kovács BSc

angestrebter akademischer Grad / in partial fulfilment of the requirements for the degree of

Master of Science (MSc)

Wien, 2024 / Vienna, 2024

Studienkennzahl lt. Studienblatt / degree programme code as it appears on the student record sheet:	UA 066 862
Studienrichtung lt. Studienblatt / degree programme as it appears on the student record sheet:	Master of Chemistry
Betreut von / Supervisor:	Univ.-Prof. Dipl.-Chem. Dr. Christian Schröder

Abstract

The influenza A virus is a major cause of seasonal flu epidemics. The virus relies on the functionality of the M2 proton channel for replication, making it a crucial target for antiviral drug development. The aim was to enhance understanding of this channel by simulating its proton transfer mechanism using a reactive water model within classical molecular dynamics and the `protex` framework. `protex`is a python-based tool to enable proton transfers between molecules in molecular dynamics simulations. Consequently, time-consuming quantum mechanical simulations of these reactions become obsolete to some extent. A key development in this research was the creation of the Drude Reactive Ionizable Polarizable Water (DRIP) model, designed to describe proton transfers in `protex` . Polarizable molecular dynamics simulations were conducted to observe the channel's behavior under various protonation states, revealing that the channel maintains an open conformation with three or four protonated histidine residues. These findings align with results from other experimental and computational studies, demonstrating that even with polarizable force fields and the new water model, the channel's functional dynamics can be effectively simulated and understood.

Contents

1. Introduction

Influenza A virus is a significant pathogen that is responsible for seasonal flu epidemics. For viral replication, it relies on the functionality of the M2 proton channel. Therefore, the transmembrane part of the M2 channel (see Figure 1.1) is a critical target for antiviral drug development and has been the subject of extensive research, particularly in understanding its proton transfer mechanisms. In these studies, various computational techniques, such as molecular dynamics (MD) and hybrid quantum mechanics/molecular mechanics (QM/MM) simulations, have been used to investigate the atomistic details of the channel's function.

In 2010, Hong and colleagues[1] utilized solid-state NMR to elucidate a proton conduction mechanism, revealing how pH changes impact the channel's structure and function. At higher pH levels, the formation of densely packed CH-π stacks by neutral histidine residues (imidazoles) inhibits the creation of an H-bonded water chain. Conversely, at lower pH, protonation leads to imidazolium formation, expanding the pore and facilitating water infiltration and proton transfer through a dynamic mechanism involving microsecond ring rotations of imidazoliums. Further insights were provided by Hong in 2012[2], using magic-angle-spinning solid-state NMR spectroscopy. This study highlighted the interactions between His37 and water, emphasizing the role of Trp41 in moderating the proton exchange rate and challenging existing models of proton conduction in the M2 channel. Williams[3] in 2012 contributed to the debate on His37's interaction mechanisms, using solid-state NMR to demonstrate that His37 forms conventional hydrogen bonds with water rather than low-barrier hydrogen bonds with other histidines, supporting the His–water proton exchange model. Dyer[4] in 2017 introduced a novel approach combining laser-induced pH jump and time-resolved fluorescence spectroscopy. This study observed rapid protonation of His37 and subsequent conformational changes, suggesting a potential role for Asp24 residues in proton collection and challenging the transporter-like mechanism of the M2 channel. Finally, Cross[5] in 2020 employed 2D J-resolved NMR spectrum analysis to investigate the His37 tetrad in the M2 protein. The study confirmed the presence of heterogeneous imidazole-imidazolium hydrogen bonds, supporting the low-barrier hydrogen bond proton conductance mechanism, and suggested new avenues for refining local structural models in diverse settings. These experimental studies collectively enhance the understanding of the M2 channel's proton transfer mechanism, providing a solid foundation for further computational and theoretical explorations.

A series of MD and QM/MM simulations have been performed by Klein and co-workers[6–9], who investigated the dynamics of proton transport and the structural stability of the M2 channel under various pH conditions. In particular, in Ref. 9, classical and hybrid QM/MM MD simulations were used to study different pH conditions, focusing on the role of water molecules and the four histidine residues His37 in the proton transport

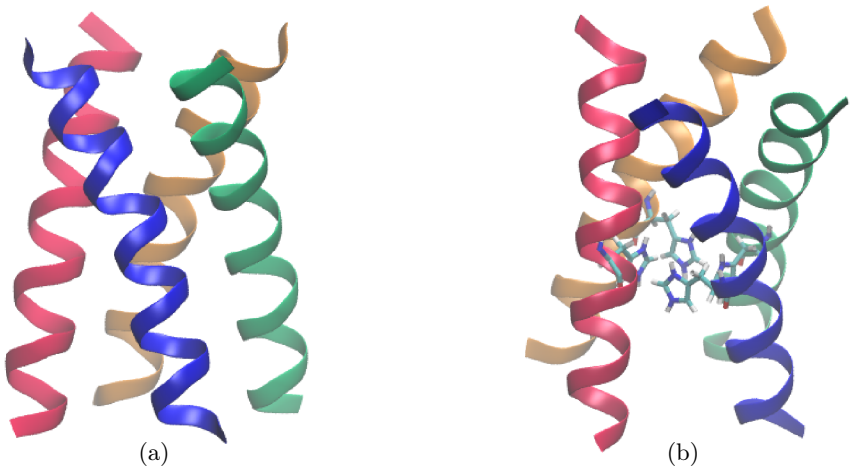

(a) (b)

Figure 1.1.: (a) Transmembrane part of the M2 Channel structure (PDB:3LBW). The helix A is colored blue, helix B red, helix C orange, and helix D green. (b) The M2 Channel structure (PDB:3LBW) including the His37 residues

mechanism. Unique configurations of pore water molecules in the channel, which formed layered structures bound by strong hydrogen bonds, were found. These structures were hypothesized to play a role in temporary proton storage. Examination of the movement and dynamics of positive charges within these water clusters suggested a smooth free-energy landscape for displacing a classical hydronium-like moiety, with certain channel regions being more favorable for cation diffusion.

Subsequent studies investigated the behavior of the channel in different protonation states, the interaction between water molecules and histidine residues, and the influence of these factors on the conformation of the channel and on the proton conduction mechanism. For example, Ref. 10 indicated that the channel remains closed in the 0, +1, and +2 protonation stages of the four His37, and only opens as the membrane undergoes further histidine protonation to the overall +3 and +4 protonation states. This opening is attributed to electrostatic repulsion among charged histidine residues, which affects the distance between nearby protein α-helix backbones.

In 2013 and 2014, Klein continued to explore the M2 channel using QM/MM simulations.[11,12] These studies confirmed the stability of different models for the His37 tetrad at neutral pH through QM/MM simulations. The His37 tetrad includes all four histidine residues of the four helices. They proposed a multiconfigurational model for proton conduction, suggesting that the channel can stabilize two protons in various configurations. In Ref. 13, constant pH MD simulations were utilized, providing insights into the pKa values of the His37 tetrad and the thermodynamics of its protonation, thereby offering explanations for the onset of proton conduction between different protonation states. In Ref. 14 and 15, extensive simulations were conducted, including the potential of mean force calculations and multiscale reactive MD simulations, to provide a comprehensive free-energy profile for proton permeation and to explore molecular interactions during

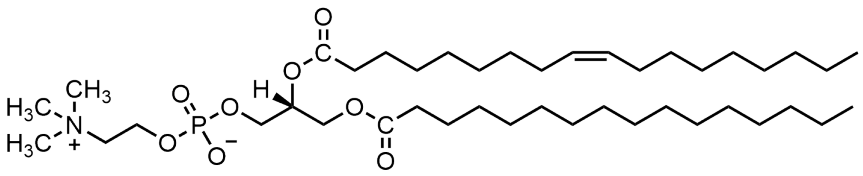

Figure 1.2.: Structure of 1-palmitoyl-2-oleoylphosphatidylcholine (POPC)

proton transport in various charge states of the His37 tetrad.[14,15] In 2020, the focus shifted to how adamantyl amine inhibitors impact proton transport, providing insights for drug development[16]. The most recent study in 2022 investigated the effects of the D44N mutation on proton transport, offering new perspectives on the significance of specific mutations in the channel's functionality[17].

The studies so far employed either classical MD or hybrid QM/MM simulations. While classical MD simulations have low computational cost, they do not allow the explicit simulation of proton transfer reactions. In contrast, hybrid QM/MM approaches can, in principle, give a detailed description of such processes. However, due to their larger computational costs, they are affordable only for short simulation times, thus limiting the sampling of these reactions. In addition, they require the manual selection of the QM region, which is further limited to only a few residues. Therefore our group has developed a program called `protex`[18], which is an efficient and cost-effective alternative to QM/MM for simulation proton transfer reactions. First, potential energy scans are performed using ab initio QM methods to determine the distances at which the transfer reactions can occur with precalculated probability based on the energy barrier between the protonated and deprotonated states. Then `protex` uses OpenMM[19] to run classical MD simulations, allowing stochastic proton transfer after specific time intervals. To use `protex` for the proton transfer between water/oxonium ions and the histidine residues of the M2 channel, we developed a unique tetrahedral water model with two dummy atoms, which can simulate both H_2O and H_3O^+ states of water molecules. The tetrahedral geometry allows for the equal treatment of the hydrogens. The `protex` model can dynamically switch between both states ("hydrogen on/off") and enables an accurate yet cost-effective representation of proton transfer reactions.

This work investigates the behavior of the M2 channel under different protonation states of histidine residues. Previous experimental and theoretical studies observed that the channel remains open with three or four protonated histidines but begins to close with fewer protonated residues. Elucidating this phenomenon is crucial for understanding the proton conduction mechanism. For this, the present work aims to provide a comprehensive simulation of the M2 channel embedded in a lipid-bilayer POPC membrane environment (see Figure 1.2) and surrounded by water. This setup models the channel's function in a biologically relevant context. Furthermore, the success of the `protex` protocol could open new avenues for studying other proton transfer mechanisms, such as those in the less explored Hv1 human proton channel[20,21], as a more accessible and cost-effective alternative to traditional classical MD and hybrid QM/MM methods.

2. Theoretical Background

2.1. Classical Molecular Dynamics

Molecular dynamics (MD) simulations provide a powerful tool to investigate molecular motion on an atomic scale, offering insights into processes such as reaction mechanisms, drug pathways, and the atomic interactions that lead to bulk properties like conductivity or diffusion. Processes occurring at the atomic scale adhere to the principles of quantum mechanics (QM). By solving the Schrödinger equation, one obtains wave functions. Often, the motion of atomic nuclei can be approximately described using classical mechanics, specifically Newton's laws, in a method known as molecular dynamics (MD).[22] The potentials that influence the movement of these nuclei are determined by the behavior of electrons. These electrons can be explicitly described using quantum mechanics in a combined approach known as ab initio molecular dynamics. Alternatively, they can be represented by parametrized, effective interactions found in what are known as force fields. These force fields form the foundation of classical molecular dynamics. While QM offers a deep understanding of electronic interactions, MD's classical treatment dramatically reduces computational costs, enabling the simulation of much larger systems over extended time scales.[23]

In classical MD, the atoms in a system under investigation (particles) obey Newton's second law of motion.[22] The force F acting on a particle i pushes it in a particular direction, as described by:

$$F_i = m_i \frac{d^2 R_i}{dt^2} \tag{2.1}$$

where m_i and R_i denote the particle's mass and position, respectively, and t is the time coordinate. The force exerted on a particle is not only influenced by its own position but also by the positions of all other particles in the system, making it a function of the entire environment. This force is the negative gradient of the potential V[22]:

$$F_i = -\nabla_i V \tag{2.2}$$

In MD, the potential is typically derived from force fields that describe the atomic interactions.[24] To simulate the motion of molecules, integration methods are employed that break down the equations of motion into small time intervals. After each interval, the equation is solved to update the positions of the particles. The choice of time step is crucial: it must be sufficiently small to capture all significant events during the simulation yet large enough to ensure reasonable computation times.[25–27]

2.1.1. Verlet Algorithm

One of the foundational methods for integrating these equations is the Euler method.[28] It is defined as

$$R_i(t + \Delta t) = R_i(t) + v_i(t)\Delta t \tag{2.3}$$

$$v_i(t + \Delta t) = v_i(t) + a_i(t)\Delta t \tag{2.4}$$

where $v(t)$ and $a(t)$ denote the particle's velocity and acceleration, respectively. However, the Euler method has its limitations. The error in this method scales quadratically with Δt, necessitating short time steps. Even with very small Δt, stability in the description of complex motion remains a challenge.

Building on the need for more accurate integration methods, the Verlet algorithm was introduced.[29] This method uses a Taylor expansion to approximate the coordinates of the next time step $t + \Delta t$ based on the positions, velocities, and accelerations of the current time step t:

$$R_i(t + \Delta t) = R_i(t) + v_i(t)\Delta t + \frac{1}{2}a_i(t)\Delta t^2 + ... \tag{2.5}$$

Analogously, the expansion is done for time $t - \Delta t$:

$$R_i(t - \Delta t) = R_i(t) - v_i(t)\Delta t + \frac{1}{2}a_i(t)\Delta t^2 - ... \tag{2.6}$$

By combining equations 2.5 and 2.6, the new positions $R(t + \Delta t)$ are obtained according to basic Verlet algorithm:

$$R_i(t + \Delta t) = 2R_i(t) - R_i(t - \Delta t) + a_i(t)\Delta t^2 \tag{2.7}$$

The velocity can then be calculated as:

$$v_i(t) = \frac{R_i(t + \Delta t) - R_i(t - \Delta t)}{2\Delta t} \tag{2.8}$$

However, the basic Verlet algorithm has some limitations. It is not self-starting, meaning that positions from the previous time step would be needed to initiate a simulation at $t = 0$. Additionally, velocities are not obtained simultaneously with the positions but only a time step later.[30] To address these issues, the Velocity Verlet algorithm was developed, which calculates positions, velocities, and accelerations concurrently. The Velocity Verlet method builds upon the principles of the basic Verlet algorithm.[31,32] Starting with equations 2.5 and 2.6, but adjusting the time t in equation 2.6 to $t + \Delta t$, we get:

$$R_i(t + \Delta t) = R_i(t) + v_i(t)\Delta t + \frac{1}{2}a_i(t)\Delta t^2 \tag{2.9}$$

$$R_i(t + \Delta t) = R_i(t) - v_i(t + \Delta t)\Delta t + \frac{1}{2}a_i(t + \Delta t)\Delta t^2 \tag{2.10}$$

Combining these equations, we derive the formula for calculating velocities:

$$v_i(t + \Delta t) = v_i(t) + \frac{1}{2}\Delta t\Big(a_i(t) + a_i(t + \Delta t)\Big) \tag{2.11}$$

The acceleration, in both the Verlet and Velocity Verlet methods, can be computed as the ratio of the force and mass of particle

$$a_i(t) = \frac{F_i(t)}{m_i} \tag{2.12}$$

2.1.2. Force Fields

A force field defines the potential energy of a system using a set of potential functions that describe how particles or atoms interact. Typically, the interactions in a force field are categorized into bonded and non-bonded terms.[24,30] The total potential energy of the system can be expressed as:

$$V = V_{bonded} + V_{non-bonded} \tag{2.13}$$

These terms are typically given by

$$V_{bonded} = V_{bond} + V_{angle} + V_{dihedral} + V_{improper} \tag{2.14}$$

$$V_{non-bonded} = V_{electrostatic} + V_{Lennard-Jones} \tag{2.15}$$

Bonded Interactions

Bonded interactions encompass the forces between atoms that are chemically bonded. They can be broken down into several components: The bond potentials describe the potential energy as a function of the bond length l between two atoms. While experimental results can be closely approximated with a Morse potential, MD simulations, especially those under equilibrium conditions, often employ the computationally efficient harmonic potential (see Figure 2.1):

$$V_{bond} = \sum_{bonds} k(l - l_{eq})^2 \tag{2.16}$$

Here, k is the bond constant, l is the current bond length, and l_{eq} is the equilibrium bond length. Angle potentials account for the energy associated with the deviation of a bond angle θ from its equilibrium value:

$$V_{angle} = \sum_{angles} k(\theta - \theta_{eq})^2 \tag{2.17}$$

Dihedrals describe the rotation around a bond, involving a chain of four connected atoms (see Figure 2.2). The potential for dihedrals is typically given by:

$$V_{dihedral} = \sum_{dihedrals} k(1 + cos(n\phi - \delta)) \tag{2.18}$$

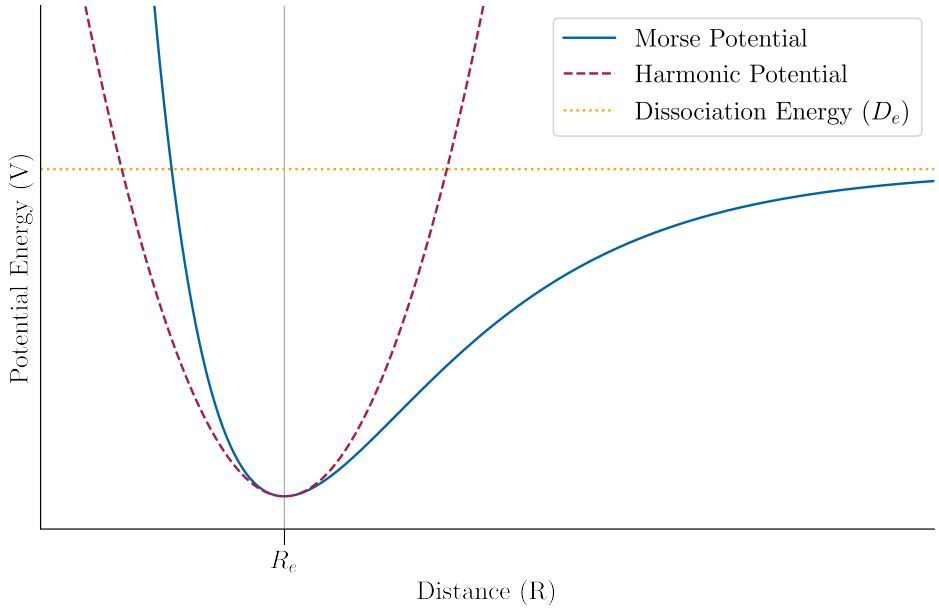

Figure 2.1.: Harmonic potential depicted in red and Morse potential shown in blue. Near the equilibrium distance, R_{min}, both potentials result in similar energy values.

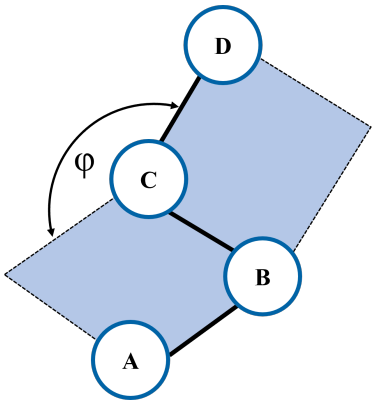

Figure 2.2.: Dihedral angle ϕ of a four atom system A, B, C and D

Where n is the multiplicity, ϕ is the dihedral angle, and δ is the phase. Improper torsions are angles defined by a plane of three atoms and a bond between the middle one of these three atoms and a fourth one. They are used in specific cases, often to maintain certain geometries:

$$V_{improper} = \sum_{impropers} k(\omega - \omega_{eq})^2 \tag{2.19}$$

Non-bonded Interactions

Non-bonded interactions encompass two primary forces: Lennard-Jones (LJ) and electrostatic interactions. Together, they are represented by the equation:

$$V_{non-bonded} = \sum_i \sum_{j>i} 4\epsilon_{ij} \left[\left(\frac{\sigma_{ij}}{R_{ij}} \right)^{12} - \left(\frac{\sigma_{ij}}{R_{ij}} \right)^{6} \right] + \sum_i \sum_{j>i} \frac{q_i q_j}{4\pi\epsilon_0 R_{ij}} \tag{2.20}$$

The first double sum of equation 2.20 is used to treat van der Waals interactions in the form of the LJ potential, which can be seen in Figure 2.3. Here, ϵ represents the depth of the potential well, indicating the strength of the interaction. σ denotes the distance at which the potential is zero, corresponding to the point where the interaction switches from repulsion to attraction. The R^{-6} term is justified by London dispersion forces, and the R^{-12} term is a computationally convenient representation of the Pauli repulsion at short ranges. Parameters ϵ and σ are typically derived from atomic parameters for each atom pair using specific rules. In the CHARMM force field, σ is often replaced by:

$$R_{min} = 2^{1/6}\sigma \tag{2.21}$$

The second term of the equation represents electrostatic interactions that arise due to the Coulomb forces between charged particles (see Figure 2.4). q_i and q_j are the partial atomic charges of the interacting atoms, R_{ij} is their separation, and ϵ_0 is the permittivity of vacuum. These charges are typically obtained through quantum mechanical methods, fitting to the electrostatic potential (ESP) of a molecule.[33,34] In managing these interactions, particularly for large systems, a concept known as the cutoff radius is employed. This is a predefined distance beyond which the non-bonded interactions like LJ and electrostatic forces are not considered in the calculations. Implementing a cutoff radius balances computational efficiency and the accuracy of the simulation, as interactions beyond this radius are deemed to have negligible impact.

2.1.3. Periodic Boundary Conditions

In MD simulations, periodic boundary conditions (PBCs) are a widely adopted technique to emulate infinite systems and mitigate surface effects. The primary objective of PBCs is to model an infinite system by replicating the simulation box, known as the unit cell, in all directions. This approach ensures that particles at the boundaries of the simulation box can interact with their counterparts on the opposite edge, providing a continuous and seamless environment for the simulated particles.[35] The fundamental idea behind

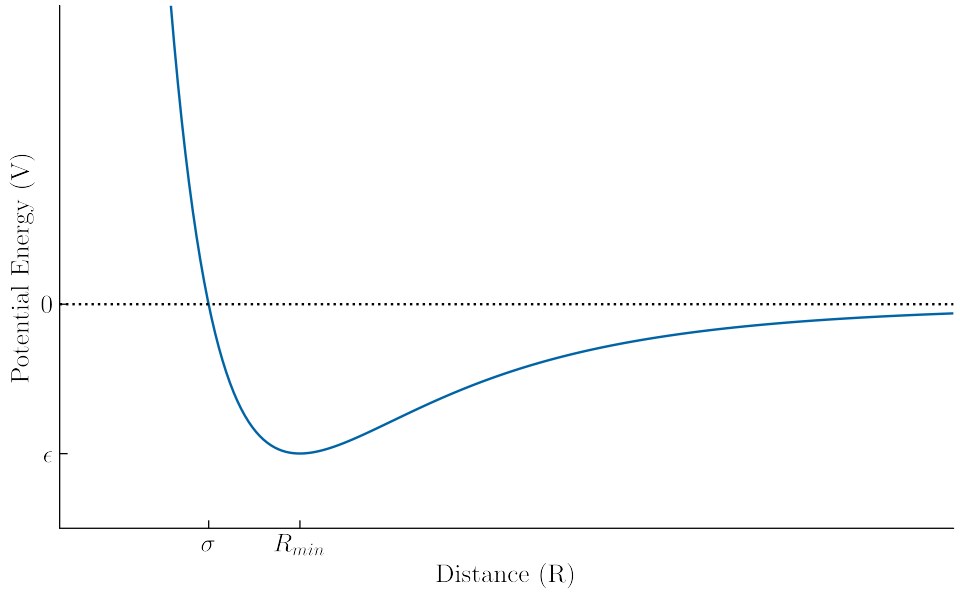

Figure 2.3.: Lennard-Jones potential

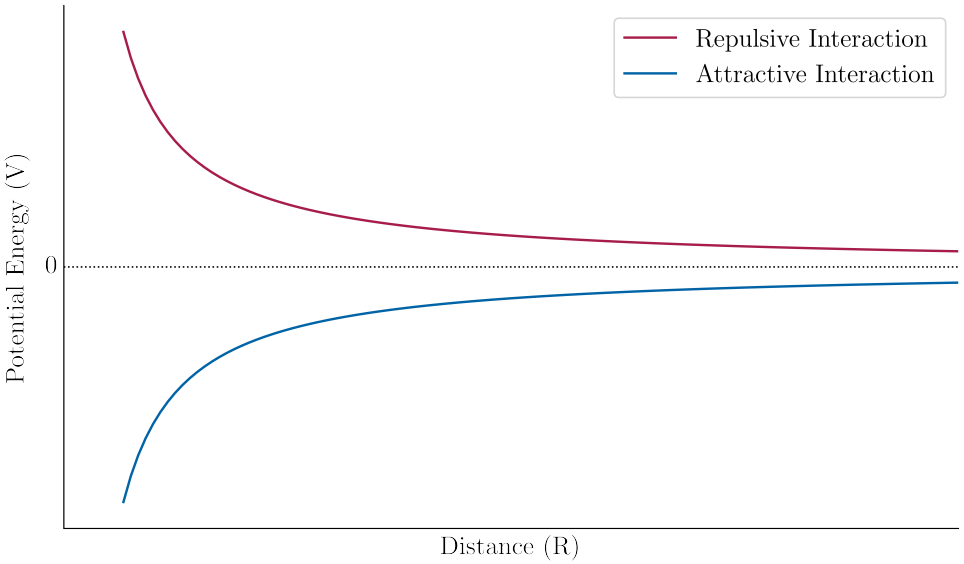

Figure 2.4.: Repulsive (red) and attractive (blue) interactions of the Coulomb potential.

PBCs is that when a particle exits the simulation box from one side, an identical copy of that particle enters from the opposite side. This ensures a constant number of particles throughout the simulation, effectively mimicking bulk conditions. The concept is depicted in Figure 2.5 for a two-dimensional system, but it extends naturally to three dimensions. Most simulations employ cubic unit cells due to their simplicity and symmetry.[27]

For interactions with a defined cutoff, such as van der Waals forces, the minimum image convention is applied. This convention ensures that interactions are only computed between the nearest atom or its periodic image, provided it lies within the cutoff distance. As illustrated in Figure 2.5, this method requires that the simulation box length is at least twice the van der Waals cutoff to maintain accuracy.

Electrostatic interactions, characterized by their $1/R$ decay, pose a significant challenge in the context of periodic boundary conditions (PBCs). Unlike van der Waals forces, which decay more rapidly ($1/R^6$), electrostatic forces diminish slower, which means that electrostatic forces extend over longer distances, transcending beyond the nearest periodic images. Consequently, the minimum image convention, effective for van der Waals interactions, becomes inadequate for electrostatic forces. In such scenarios, simply considering the nearest image or relying on a limited cutoff radius fails to capture the full extent of these long-range interactions. This inadequacy necessitates including more distant periodic copies to accurately account for the influence of electrostatic forces.

To address this issue, advanced techniques like the Ewald summation are employed. Originally formulated for ionic crystals, the Ewald summation technique enables the efficient and precise calculation of electrostatic interactions in periodic systems, encompassing contributions from multiple periodic images. In contemporary simulations, a variation known as the Particle Mesh Ewald (PME) method is more commonly used. PME offers an efficient approach to handle long-range electrostatics, ensuring accuracy and computational feasibility.[22]

2.1.4. Polarizable Molecular Dynamics Simulations

The electron density and polarization effects are not explicitly considered in MD simulations, leading to potential inaccuracies in certain scenarios like interactions of induced dipoles. To address this, the concept of polarizable charges is introduced, allowing for a more realistic representation of molecular interactions.

Classical or additive force fields typically employ fixed partial charges for atoms. This approach, while computationally efficient, can not model interactions of induced dipoles as the dipole moment remains static and unresponsive to environmental changes. Polarizable force fields address this limitation by making the electrostatic properties of atoms flexible. Polarization describes the change in charge distribution in response to an external electric field. In essence, it captures the ability of a molecule to reorient its charge distribution in the presence of an external electric field. This phenomenon is crucial for accurately modeling interactions, especially in systems like ionic liquids, where the absence of polarizability can lead to unrealistic dynamics.[36,37]

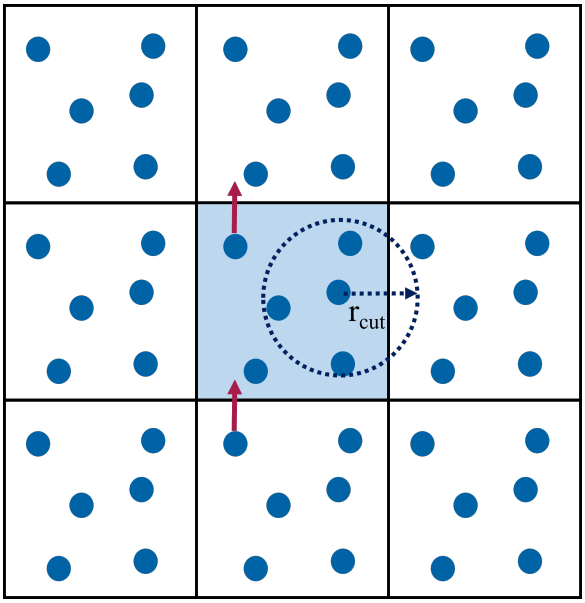

Figure 2.5.: Simulation box colored light blue, featuring periodic boundary conditions in two dimensions. The dashed circle demonstrates the cutoff distance of a particle with other particles. Red arrows illustrate a copy entering the simulation box when its original particle exits it.

Drude Oscillator Model

One of the most prevalent methods to introduce polarizability in MD simulations is the Drude oscillator model (see Figure 2.6).[38–40] In this approach, an additional particle, termed the Drude particle, is bound to each polarizable atom via a harmonic potential. This Drude particle typically carries a negative charge, representing an electron cloud. By allowing the Drude particle to react to external electric fields, the atomic dipole moment can adapt to environmental changes.

The atomic dipole moment μ_i, is defined as:

$$\mu_i = \alpha_i \cdot E_i = \frac{q_D^2}{k_D} E_i \tag{2.22}$$

where α_i is the atomic polarizability, defined by the force constant k_D and the charge of the Drude particle q_D, while E_i is the external electric field at the position of the atom i. The Drude model represents the polarized electron cloud by displacing the Drude particle relative to its parent atom characterized by the vector d_i. This displacement creates a physical dipole:

$$\mu_i^{ind} = -q_D R_i + q_D(R_i + d_i) = q_D\, d_i \tag{2.23}$$

Implementing the Drude model requires additional computational considerations. One approach is the self-consistent field method, which, while accurate, can be computationally expensive. An alternative is the extended Lagrangian with dual thermostats method,

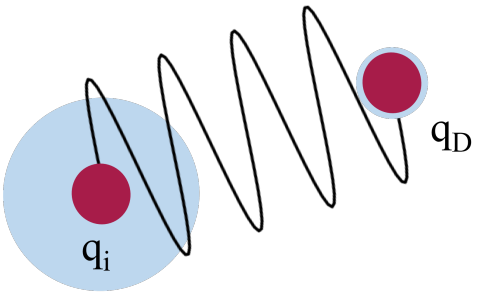

Figure 2.6.: A Drude particle is attached to an atom via a harmonic potential. The charges of these particles are indicated in red.

which treats Drude particles with Newtonian mechanics, similar to other atoms in the system.[41,42]

2.2. Simulating Proton Transfer Reactions

Classical MD simulations, defined by the fixed connectivity of their atoms and typically modeled by harmonic bond potentials, cannot handle bond breaking or formation. This limitation necessitates specialized tools for simulating reactions, such as proton transfer.[43,44]

`protex` is an advanced simulation tool designed to address this challenge and works seamlessly with the MD packages CHARMM[27] and OpenMM.[19] It employs a single topology approach, where deprotonated molecules retain a placeholder or "dummy" hydrogen with no charge.[45] This design facilitates instantaneous proton transfer, ensuring an accurate representation of dynamic properties like diffusion or conductivity.[18] However `protex` is not limited to ionic liquids.

The architecture of `protex` is divided into the ProtexSystem and Update classes.[18] The ProtexSystem class combines the simulation object with additional information on the update process. The Update class manages the logic during an update, ensuring accurate simulation of proton transfers. The probability and distance for proton transfers in `protex` are derived from QM scans.[46] Relaxed, one-dimensional scans along the proton transfer coordinate, such as along an O−H axis, offer insights into transfer energetics. The transformation of these barriers into reaction probabilities, p, is realized through several models: One such model – employed in this thesis – is based on the kinetic energy, E_{kin}, of the protonated molecule. Its normalized Maxwell–Boltzmann distribution is given by:[46]

$$f(E_{kin}) = \frac{E_{kin}}{(k_B T)^2} \exp^{\left(-\frac{E_{kin}}{k_B T}\right)} \tag{2.24}$$

The percentage of these molecules is calculated using the normalized distribution, resulting

in the probability:

$$p(E_{kin}) = \int_{E_{kin}}^{\infty} f(E_{kin}) dE_{kin} \tag{2.25}$$

After conducting a proton transfer with `protex`, proton transfer between the same residues is prohibited for the next 10 updates. In this context, this prohibition equates to a duration of 50 ps. This measure is implemented since these two residues are in close proximity, which helps to avoid constant proton transfer between them.

In this thesis, `protex` was employed to simulate proton transfer reactions in proton channels between water and different amino acids.

2.3. Analysis

2.3.1. Radial Distribution Functions

The radial distribution function (RDF), denoted as $g(r)$, provides insights into the structural arrangement of a system at the microscopic level. It quantifies how particle density varies as a function of distance from a reference particle,[31,47] which can be represented by atomic positions or by the center of mass of a molecule. The number of neighboring particles of a particular species within concentric shells around this reference is counted and subsequently averaged. This count is mathematically represented by[48]:

$$n(R) = \left\langle \frac{1}{N_i} \sum_{i=1}^{N_i} \sum_{j \neq i}^{N_j} \delta\left(|R - R_{ij}|\right) \right\rangle \tag{2.26}$$

To obtain the classical RDF $g^{000}(R)$, the count $n(R)$ is normalized by the shell thickness, $4\pi R^2 \Delta R$, and the overall particle density ρ_j:

$$g_{ij}^{000}(R) = \frac{1}{4\pi R^2 \Delta R \cdot \rho_j} \cdot n(R) \tag{2.27}$$

The RDF offers a way to explore the average number of particles surrounding each species based on their radial distance. This facilitates the determination of coordination numbers and the average separation between particles. A characteristic feature of the RDF is its zero value at $R = 0$ because no particle can occupy the same position as the reference. As R increases to large distances, the RDF tends towards one, indicating that the local density converges to the average system density. The distinct peaks observed between these two limits correspond to coordination shells, revealing the preferred particle separations.[22,47]

In addition to $g^{000}(R)$, one can also compute the $g^{110}(R)$ function, which gives information about the mutual orientation of the molecules i and j

$$g_{ij}^{110}(R) = \frac{1}{4\pi R^2 \Delta R \cdot \rho_j} \cdot \left\langle \frac{1}{N_i} \sum_{i=1}^{N_i} \sum_{j \neq i}^{N_j} \cos(\mu_i, \mu_j)\ \delta(|R - R_{ij}|) \right\rangle \tag{2.28}$$

characterized by their dipole moments μ_i and μ_j. If $g^{110}(R)$ is negative, the molecules tend to be orientated antiparallel. If $g^{110}(R)$ is positive, a parallel alignment is preferred.

2.3.2. Root Mean Square Deviation

The root mean square deviation (RMSD) is a widely used measure in molecular dynamics to quantify the deviation of a current structure from a reference structure over time. For a group of N atoms, the RMSD $\rho(t)$ at time t is defined as:[49]

$$\rho(t) = \sqrt{\frac{1}{N}\sum_{i=1}^{N} w_i \left(R_i(t) - R_{\text{ref},i}\right)^2} \tag{2.29}$$

where $R_i(t)$ is the position of atom i at time t, $R_{\text{ref},i}$ is the position of atom i in the reference structure and w_i are the weights for each atom. The weights w_i are derived from the input weights w_i' as relative to the mean of the input weights:

$$w_i = \frac{w_i'}{\langle w' \rangle} \tag{2.30}$$

RMSD facilitates the comparison of the protein's dynamic structures against a reference structure, which is essential for assessing changes and stability in protein conformation during molecular dynamics simulations.

2.3.3. Diffusion

Diffusion is a fundamental transport process where molecules move, typically along a concentration gradient. This movement is often driven by the inherent kinetic energy of the molecules and their interactions with neighboring molecules. The flux J of particles, which represents the rate of diffusion, is influenced by the concentration gradient and is described by Fick's first law:

$$J = -D\frac{dN}{dx} \tag{2.31}$$

Here, $\frac{dN}{dx}$ represents the change in particle number along a specific direction x. The proportionality constant D is the diffusion coefficient.[50] The time-dependent nature of diffusion is captured by Fick's second law, which relates the rate of change in concentration over time to the spatial change in concentration at a specific point:

$$\frac{\partial N}{\partial t} = D\frac{\partial^2 N}{\partial x^2} \tag{2.32}$$

D is a crucial material constant that quantifies the rate of diffusion. It can be derived using various approaches. One common method is the Einstein-Helfand approach, which utilizes the mean squared displacement (MSD) of the trajectory:[31]

$$D = \frac{1}{6}\frac{d\left\langle \Delta R^2(t) \right\rangle}{dt} \tag{2.33}$$

Where the mean squared displacement at a given time t is defined as:

$$\left\langle \Delta R^2(t) \right\rangle = \left\langle \frac{1}{N}\sum_{i=1}^{N} \Big(R_i(t) - R_i(0) \Big)^2 \right\rangle \tag{2.34}$$

After the initial ballistic regime, the MSD increases linearly with time, allowing the diffusion coefficient to be determined from the slope of its linear region.[22]

Another approach to determine the diffusion coefficient is the Green-Kubo relation, which is based on the correlation function of particle velocities over time:

$$D = \frac{1}{3} \int_0^\infty \langle v_i(0) \cdot v_i(t) \rangle \, dt \tag{2.35}$$

This relation emphasizes that as particles move and collide over time, their velocities become less correlated with their initial velocities, leading to a correlation function approaching zero.[31] In simulations, especially those using periodic boundary conditions (PBC), care must be taken when calculating diffusion coefficients. To address issues arising from PBC, trajectories must be unfolded, ensuring that particle positions are not translated to the opposite side of the simulation box before analysis in order to avoid unphysical jumps.

2.3.4. Dielectric Spectrum

Dielectric spectroscopy is a technique employed for systematically exploring material electrical properties, which are its permittivity ϵ and conductivity σ. They are inherently influenced by factors such as composition, temperature, and the frequency of the applied electric field.[51] The permittivity ϵ is a fundamental parameter that quantifies a material's responsiveness to an electric field, representing its inherent capacity to store electrical energy when subjected to such a field. Materials exhibiting high dielectric constants demonstrate superior insulating properties, while those with lower dielectric constants display poor insulating characteristics. Permittivity is conventionally represented as a complex quantity, comprising a real component ϵ' and an imaginary component ϵ'':

$$\epsilon^*(\omega) = \epsilon'(\omega) - i\epsilon''(\omega) \tag{2.36}$$

Here, $\epsilon^*(\omega)$ denotes the complex dielectric permittivity, $\epsilon'(\omega)$ corresponds to the energy storage capacity per period, and $\epsilon''(\omega)$ signifies the energy dissipation per period.[52]

Dielectric spectroscopy serves as a comprehensive tool for characterizing the response of materials to electric fields of varying frequencies from millihertz to the gigahertz regime and even beyond, with a particular focus on elucidating their molecular and structural attributes, along with their interactions with electromagnetic radiation.[53] For example, smaller molecules may rotate faster and consequently can align their dipole moments to the external field more quickly. Molecules with neither a charge nor a dipole moment do not possess a dielectric spectrum.

In the realm of computational chemistry, the complex permittivity can be determined based on the total collective dipole moment as:

$$M_{tot}(t) = \sum_i \sum_\beta q_{i\beta} \cdot r_{i\beta}(t) \tag{2.37}$$

Here, i is the molecular and β the atomic index, respectively. The total collective dipole moment is further dissected into a translational component $M_J(t)$ and a rotational component $M_D(t)$:

$$M_J(t) = \sum_i \sum_\beta q_{i\beta} \cdot r_{com,i}(t) = \sum_i q_i \cdot r_{com,i}(t) \tag{2.38}$$

$$M_D(t) = M_{tot}(t) - M_J(t) = \sum_i \sum_\beta q_{i\beta} \cdot \Big(r_{i\beta}(t) - r_{com,i}(t) \Big) \tag{2.39}$$

where $r_{com,i}(t)$ represents the position of the center of mass of molecule i, and q_i denotes its molecular charge, which is the sum of the atomic charges $q_{i\beta}$ of that molecule. The collective rotational dipole moment M_D captures all non-translational molecular motions, i.e., rotations and vibrational modes.[54]

Using these definitions, the collective dipoles can also be calculated for charged systems. Neutral molecules, like water, contribute to the dielectric spectrum via their rotation captured by the autocorrelation function of the collective rotational dipole moment $\langle M_D(0) \cdot M_D(t) \rangle$. Simple ions without a dipole moment contribute via their translation characterized by the collective translational dipole moment M_J. Molecular ions with a dipole moment, like most of the ionic liquid cations and anions, contribute via both channel, rotation and translation.

Since we are dealing with water in a protein channel, the translational part of the dielectric spectrum only plays a marginal part and can be neglected here. Consequently, the permittivity reads:

$$\epsilon(\omega) - \epsilon_\infty = \frac{4\pi}{3Vk_BT} \mathcal{L} \left[-\frac{d}{dt} \langle M_D(0) \cdot M_D(t) \rangle_{eq} \right] \tag{2.40}$$

applying linear response theory.[52]

The high-frequency limit ϵ_∞ represents the response of the material beyond the movement of the atoms, i.e. electronic deformations as a function of the electric field. In non-polarizable MD simulations, this value is set to unity. In polarizable simulations, the high-frequency limit can be obtained via:

$$\frac{\epsilon_\infty - 1}{\epsilon_\infty + 2} = \frac{4\pi}{3} \cdot \frac{\alpha_{tot}}{V} \tag{2.41}$$

using the total polarizability of the system, which is usually the sum of all polarizabilities, and the volume V.

Since the dielectric spectrum ranges over several orders of magnitude and hence characterizes the properties of a solvent from very slow to very fast, the computational spectrum is optimal for validating the force field, particularly for water.[55]

3. Computational Details

3.1. QM Scans

The geometry optimization and the relaxed potential energy scans were performed using density functional theory (DFT)[56,57] as implemented in the Gaussian program (version 16).[58] DFT is the most common method used in quantum chemistry to solve the electronic Schrödinger equation. Unlike wavefunction theory, where energy and other properties are derived from the wavefunction, DFT expresses these properties as a function of electron density. However, since the precise form of the functional is not known, practical calculations necessitate the use of approximate exchange-correlation functionals.[56] The DFT functional B3LYP[59] with D3 dispersion correction[60,61] was employed using the 6-311++G(d,p)[62,63] basis set. Solvent effects of water were included using the implicit solvation model polarizable continuum model (PCM)[64,65]. For explicit solvation, additional water molecules were added to the simulations.

3.2. Molecular dynamics simulations of pure water

To find the optimal force field parameters for our polarizable DRIP water model, several MD simulations were performed varying several force field parameters like the Drude charge, the force constant of the angle H−O−H, the ϵ and the $R_{min}/2$ values of the van der Waals interactions.

Packmol[66] was used to set up the simulation box with 1000 DRIP molecules in it. DRIP is the water model developed in this thesis as explained in Section 4.2. After setting up the water box, CHARMM[27] was applied to create the structure file psf and coordinate files. The simulation box was set up using polarizable force fields for all particles.[39,40,67] For the simulations, the OpenMM 7.6 program[19] was used due to computational efficiency. The Drude particles had a mass of 0.4 a.u., and the maximum allowed Drude distance d_i was 0.2 Å. The SHAKE algorithm was applied to constrain all bonds involving hydrogen atoms.[68] The particle mesh Ewald (PME) was applied with an error tolerance of 0.0001 as the electrostatic cut-off method.[69,70] The force-switch method was used for cutting van der Waals interactions with a switch-on distance of 1.0 nm and a switch-off distance of 1.1 nm.

First, an NpT ensemble was simulated with a 40 ps pre-minimization and with a time step of 0.1 fs for the equilibration of the system at 1 atm and 300 K. The dual thermostat kept the atoms at this temperature while the vibration of the Drude particles was set to 1 K. After that, a time step of 0.5 fs was chosen, and the simulation box was equilibrated for 5 ns. For the production run, a 0.5 fs time step was chosen for a total simulation time

of 50 ns. In every simulation, the Velocity Verlet integrator was used from Ref. 71.

3.3. Molecular dynamics simulation of the M2 Channel

3.3.1. M2 Channel with TIP3P

OpenMM 7.6[19] was employed to run the simulations, and the input files for OpenMM were generated by CHARMM-GUI,[72,73] using the membrane builder function[74,75] with the bilayer builder option. The hydrogen coordinates were preserved from the input PDB and the protonation state of the histidine was changed from HSD to HSP as shown in Appendix A.2. The coordinates of the protein were used as in the input PDB. A heterogeneous lipid was added within a rectangular box type and 22.5 Å water layers were added at the top and the bottom of the system. The ratio of the upper and lower membrane leaflet was set to 1:1. In Figure 3.1 it can be seen how a simulation box looks like.

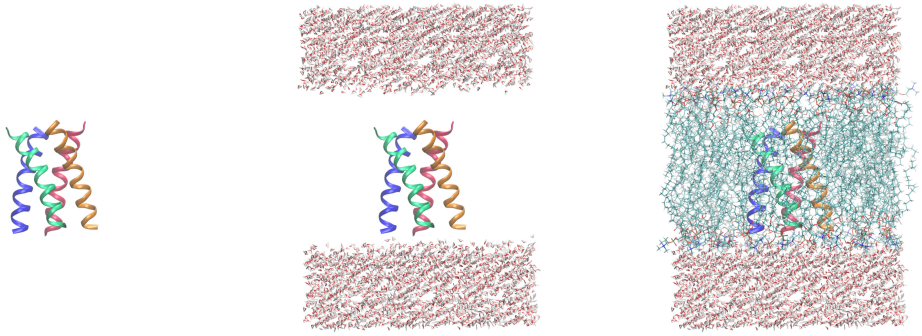

(a) (b) (c)

Figure 3.1.: Representation of a simulation. (a) Showing only the protein (b) showing the protein with TIP3P water model (c) showing the whole simulation box, with the protein embedded in the membrane surrounded with TIP3P water

Three different PDB structures were used to simulate the M2 proton channel:

- 1NYJ[76] is a closed state structure of M2 protein H^+ channel constructed from solid state NMR spectroscopic data.
- 3LBW[77] is high resolution crystal structure of transmembrane domain of M2. For our purposes the amantadine molecule was not included in the simulations.
- 2L0J[78] is structure of the entire M2 proton channel constructed from solid state NMR data.

The number of phospholipids was set to 80-130 molecules per bilayer.[79] Na^+ and Cl^- were added to the water with a 0.15 M concentration. Additional Na^+ or Cl^- neutralize the system depending on the protonation state. During this setup stage, no protein surface penetration or lipid ring penetration was observed. The simulations were run with the CHARMM36m force field[41] while using the hydrogen mass repartitioning to increase the time step.[80] The electrostatic cut-off method is PME with an error tolerance of 0.0005.[69,70] The van der Waals cut-off method is Force-switch with a switch-on distance of 1.0 nm and a switch-off distance of 1.2 nm. Positional restraint force constants for protein backbone, protein side-chain and for lipids as well as the dihedral restraint force constant for lipids were employed using the default values provided by CHARMM-GUI.

Simulations were run using the NpT ensemble at a temperature of 303.15 K and a pressure of 1 bar. After the system was equilibrated with the default values provided by CHARMM-GUI, the production run was performed using a time step of 4 fs for a total simulation time of 500 ns. The run was split into five sequential 100 ns simulations for I/O handling.

3.3.2. M2 Channel with DRIP Water Model

CHARMM-GUI was used to set up the protein and the membrane environment with the membrane bilayer tool.[72–75,79,81,82] The number of POPC molecules was set to ca. 80 molecules per bilayer.[79] Na^+ and Cl^- were added to the water with a 0.15 M concentration and additionally to neutralize the system depending on the protonation state. Packmol[66] was used to add DRIP water molecules with oxonium ions to the protein and membrane environment. For an example input file for Packmol see Appendix A.3. After setting up the simulation box, CHARMM[27] was applied to create psf and coordinate files and to make the atoms polarizable using Drude particles.[39,40,42,83–85] In these simulations, all particles except those belonging to the lipid bilayer membrane are polarizable. The further computational details concerning the actual simulation runs can be seen in the previous Section 3.2.

3.4. Analyzing the Trajectories

In this study, MDAnalysis[86,87], a Python package tailored for the analysis of molecular dynamics simulations, was extensively utilized for the examination of trajectory data. The core of our analysis involved iterating through the trajectory frames. A significant aspect of this process was computing the center of mass for selected residues within each frame. This computation was crucial for the subsequent mean squared displacement (MSD) analysis. To accurately calculate the MSD, trajectory data were first unfolded to address periodic boundary conditions. The MSD was then computed based on the center of mass positions, using the `msd_com` function. Notably, the diffusion coefficient was derived for a specific time range in the simulation, particularly between 20 to 25 nanoseconds, providing insights into the dynamic behavior of the system within this interval.

In the analysis, RMSD calculations were conducted to evaluate the dynamics of protein structures. The RMSD function from the `MDAnalysis.analysis.rms` module was used, with a focus on the protein's backbone atoms. Targeting these atoms is essential for accurately assessing conformational changes in the protein structure. To manage issues related to PBC, the `nojump.NoJump` transformation from MDAnalysis was employed. This transformation maintains the consistency of the protein structure throughout the simulation box, which is critical for accurate RMSD measurement. Alignment of the trajectory data with a reference structure was executed using the `align.AlignTraj` function. Such alignment ensures that the RMSD values obtained are in reference to a consistent structural frame, enabling the true representation of structural deviations over time.

The process of obtaining dielectric spectra from molecular dynamics simulations begins with the use of MDAnalysis for trajectory analysis. The script efficiently iterates through trajectory frames, where the `centerOfMassByResidue` and `dipoleMomentByResidue` functions calculate the center of mass and dipole moments for selected molecular species. Following this, the `correlateParallel` function is utilized to compute the time correlation functions of these dipole moments. The computed time correlation functions then serve as key inputs for the GENDICON[88]. Here, exponential fitting functions are applied to model the decay of correlations over time. GENDICON takes into account various parameters, including temperature (300 K), box dimensions (ca. 30 Å), and a defined frequency range (from 1×10^{-5} THz to 50.0 THz), to calculate the dielectric spectrum.

RDF was calculated employing MDAnalysis to process trajectory files, iterating through frames and applying the `centerOfMassByResidue` and `dipByResidue` functions to determine the center of mass and dipole moments for selected residues. These calculations provide spatial coordinates and dipole orientations necessary for RDF computation. Using the `RDF` class from the `newanalysis.gfunction` module, the script computes the RDF, which indicates spatial distribution and orientation correlations between molecules. The `calcFrame` method of the RDF class is used for each frame to build up the RDF data over the trajectory.

Lastly, the MOLE 2.0 program[89,90] was utilized to analyze the volume size of the channels. This program also offers an online tool, which is available at Ref. 91.

4. Results and Discussion

The project aims to simulate the M2 channel using a reactive water model integrated with the `protex` framework. The initial step involves conducting QM scans to obtain reaction probabilities for `protex`, which is crucial for accurate modeling. Following this, the focus is on developing a water model and to analyze how macroscopic properties such as density are influenced by atomistic force-field parameters. Afterwards the structure of the proton channel is set up for different protonation states with different water models. Different PDB structures and lipid bilayer structures are simulated to gain the best set up for further simulations. The final part includes employing the newly-developed DRIP water model in simulations of the M2 channel with different protonation states.

4.1. QM Potential Energy Scans

In this section of the work, the QM scans of the potential energy surfaces provide the probabilities for `protex` using Eq. 2.25. Current models assume that proton conduction in the M2 channel may occur via proton transfer between a doubly protonated histidine (HSP) residue and singly protonated histidine (HSD) residue supporting the low-barrier hydrogen bond proton conductance mechanism which was reported in Ref. 5. The more established models for the proton conduction are His-water proton exchange model and the water-water proton exchange model.[9] These reactions were also simulated with QM to obtain the reaction probabilities.

4.1.1. Proton transfer between histidine and histidine

In Figure 4.1 one can see the potential energy surface of the proton transfer reaction between HSP and HSD residues. The reaction shows an energy barrier of 1.7 kcal/mol. The small energy difference between initial and final step of 0.2 kcal/mol is likely due to small changes in the conformations. TThe reaction probability calculated using Eq. 2.25 is 19.81%, indicating the likelihood of this reaction occurring. Since the reactants and products are identical, the probabilities for both the forward and backward reactions are the same. For initial calculations with `protex`, the probability was set to 1 (or 100%) to facilitate observation of the reaction. This implies that the reaction occurs when the predetermined distance between the residues is met.

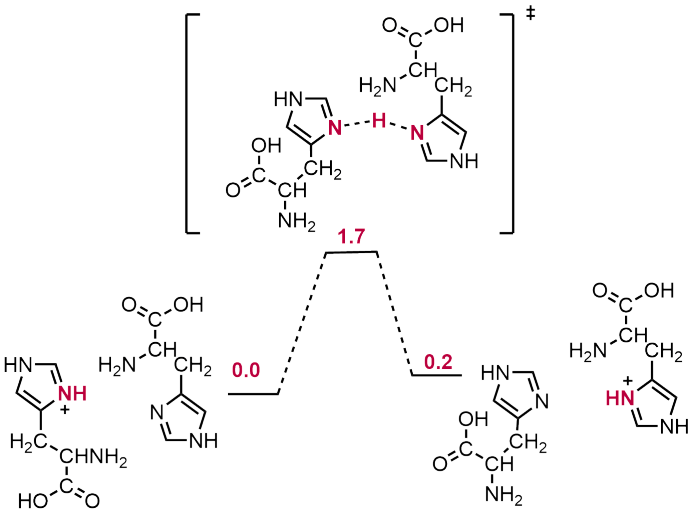

Figure 4.1.: Potential energy surface of the proton transfer reaction between a HSP and a HSD residue. The energies are given in kcal/mol.

4.1.2. Proton transfer between water molecules

As a next step the water-oxonium proton exchange was modelled. Based on Ref. 92, four water molecules were included in the simulation (see Figure 4.2). Since the H_3O^+ ion alone is not stable in aqueous solution, one has to simulate larger ionized water clusters. For example, for $H_9O_4{}^+$, there is an energy difference of 17.1 kcal/mol between the initial step and the last step of the proton transfer. This difference occurs because the water/oxonium ions participating in the reaction do not have enough other water molecules explicit in the simulation to stabilize them with hydrogen bonds. The implicit solvent modelling of water can not balance out the lacking of explicit waters. These findings indicate that more explicit water molecules, at least six should be included. As it can be seen in Figure 4.3) the energy difference dropped to +3.5 kcal/mol, because of the presence of additional water molecules. The reaction probability cannot be calculated using Eq. 2.25 due to the reaction being barrier-less. Additionally, the energy difference of 3.5 kcal/mol can be attributed to the insufficient simulation of water molecules explicitly. Consequently, the reaction probability was set to 1. The reactants and products are chemically identical, differing only in their conformation. Therefore, the forward and backward reactions should have the same probability.

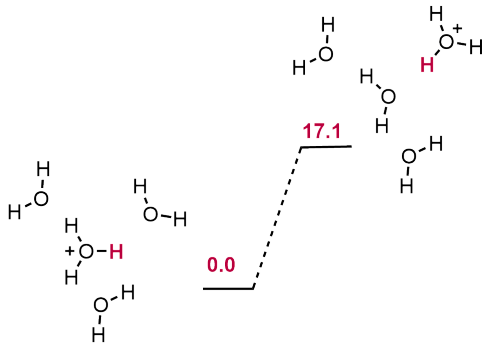

Figure 4.2.: Potential energy surface of the proton transfer reaction between water molecules, including four of them. The energies are given in kcal/mol.

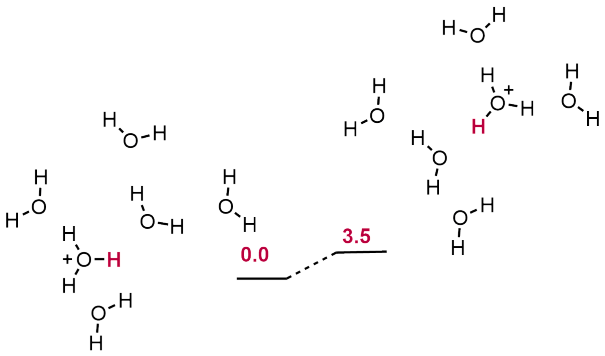

Figure 4.3.: Potential energy surface of the proton transfer reaction between water molecules, including six of them. The energies are given in kcal/mol.

4.1.3. Proton transfer between histidine and water

In Figure 4.4 the potential energy scan of the HSP-water proton transfer can be seen. The oxonium ion is less stable compared to the HSP residue, which explains why the reaction product of HSD residue and oxonium ions has 15.4 kcal/mol more energy than the reaction complex. The probability calculated with the Eq. 2.25 is 99.89% which means that the oxonium ion transfers the proton to the histidine residue if the two molecules are close enough.

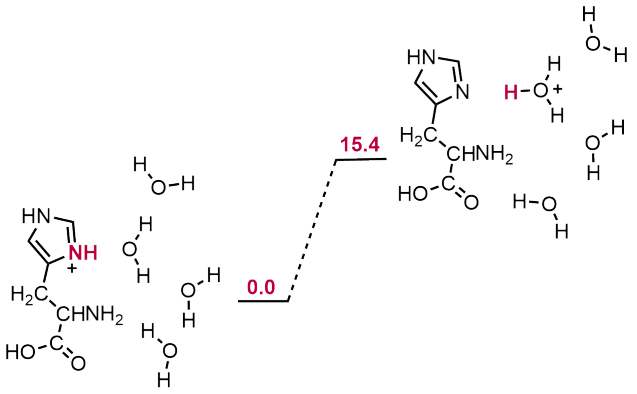

Figure 4.4.: Potential energy surface of the proton transfer reaction between HSP residue and water molecules. The energies are given in kcal/mol.

4.2. Optimizing the Water force field

In this section the water model is developed in order to simulate proton transfer reactions with `protex`. As starting model, a tetrahedral model with two hydrogen atoms was employed.[93] The tetrahedral geometry was chosen to ensure equal treatment of the hydrogen atoms. Rather than lone pairs on the oxygen, two dummy hydrogen atoms were added. These dummy atoms are essential for simulating proton transfer, and their presence allows the water to be protonated from both sides (see Figure 4.5). To develop a water able to describe proton transfer reactions, the Drude charge, the force constant of the angle H−O−H, and the van der Waals parameters were changed. The density, the dielectric constant and the diffusion coefficient of the water models were monitored to obtain the most acceptable values.

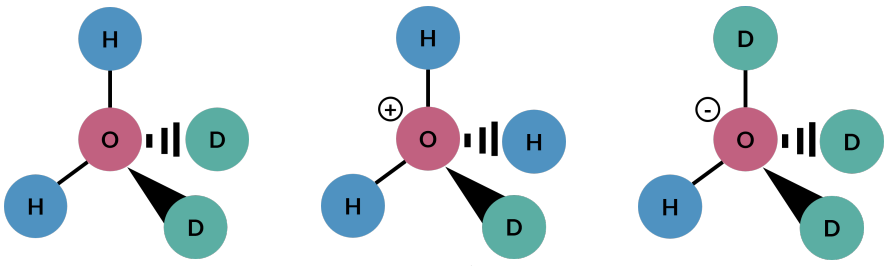

(a) H_2O (b) H_3O^+ (c) OH^-

Figure 4.5.: Tetrahedral water model with adjustable hydrogen atoms including the oxonium ion and the hydroxid form. Oxygen is depicted with red, while the hydrogens are blue and the dummy atoms are shown in green.

4.2.1. The influence of the Drude charge

In Figure 4.6 one can see the influence of changing the Drude particle charge on the density, the dielectric constant and on the diffusion of water. As the charge on the Drude particle increases (becoming more negative), the density of the system dramatically increases (from 1.0046 to 1.2092 g/ml). This trend, which is somewhat unexpected, suggests that greater polarization, as indicated by a larger negative charge on the Drude particle, leads to stronger intermolecular interactions and, consequently, a more compact arrangement of water molecules. Typically, one would expect that a smaller Drude charge would correlate with a larger distance between the Drude particle and the polarizable atom, but in this instance, the Drude hardwall (0.2 Å) may have prevented the distance from increasing. As a result, the induced dipole becomes smaller, contrary to what might be anticipated under normal circumstances. The increase in density indicates that the water molecules are able to pack more closely as the polarization effects become more pronounced. The dielectric constant increases markedly with larger negative values in the Drude charge. This is consistent with the understanding that polarization contributes significantly to the dielectric response of a material. Higher polarization enhances the ability of the water molecules to orient themselves in an electric field, thus increasing the dielectric constant. The diffusion coefficient decreases as the Drude charge becomes more negative. This is typically the case since diffusion often shows a trend opposite to that of density; more densely packed systems move much slower. Additionally, small changes in density can have significant effects on the dynamics. This indicates that increased polarization leads to reduced mobility of the water molecules. This could be due to stronger dipole-dipole interactions and more significant hydrogen bonding in the presence of increased polarization, which would hinder the movement of the water molecules through the liquid.

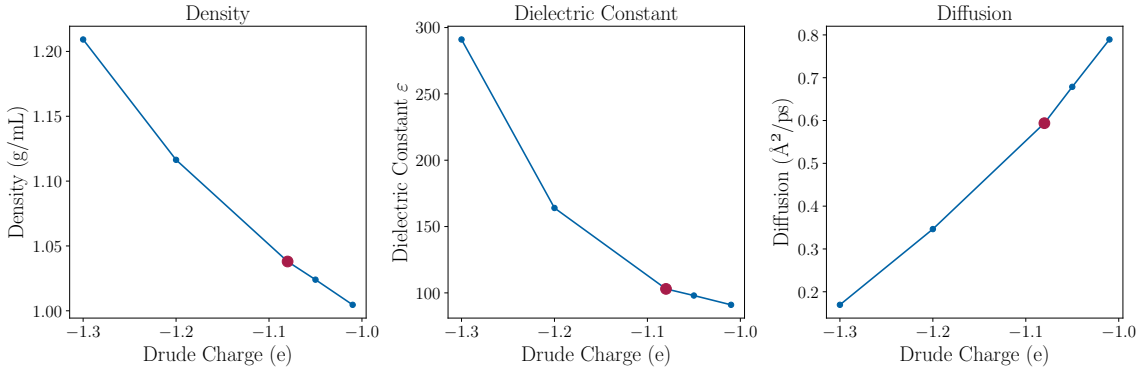

Figure 4.6.: The three figures show the effect of changing the charge of the Drude particle on the density, the dielectric constant and on the diffusion of water. The red points indicate the value that was taken for the water model.

4.2.2. The influence of the water angle

Figure 4.7 shows how the force constant of the H−O−H angle influences the density, the dielectric constant and the diffusion of the water molecules. The angle between the

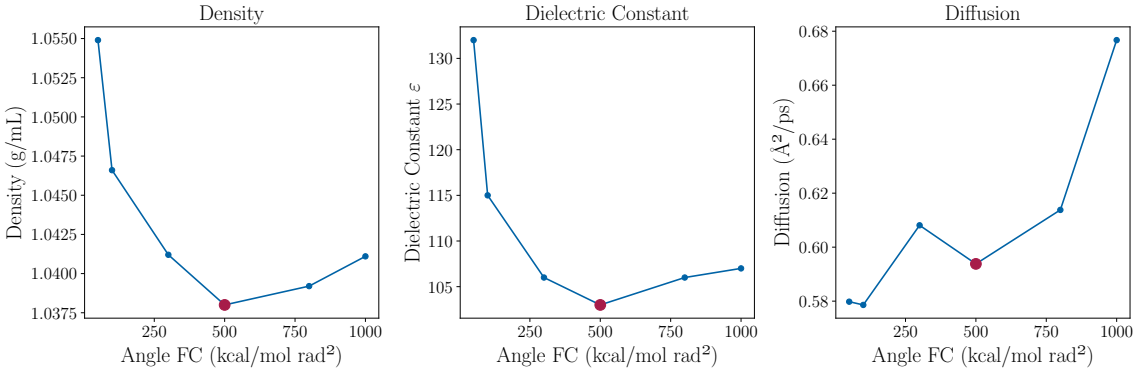

Figure 4.7.: The three figures show the effect of changing the force constant of the angles between the oxygen and the hydrogen atoms, on the density, the dielectric constant and on the diffusion of water.

hydrogens and the oxygen is 109.45°. If the force constant is weak, it allows to deform the tetrahedral angle which leads to higher density and as well larger dielectric constant. However as it can be seen in the curves of the density and the dielectric constant, the trend has a minimum around 500 kcal/mol rad^2 and if the force constant is increased up to 1000 kcal/mol rad^2, the curves show again an increase in both the density and the dielectric constant. This can mean that the force constant is so strong that it does not allow any bending of the angle anymore. The diffusion of water exhibits an overall increase with an increasing force constant, which is counter-intuitive; one would typically expect that stiffer molecules would have more difficulty passing each other.

4.2.3. The impact of the Lennard-Jones parameters

Figure 4.8 shows how the density, the dielectric constant and the diffusion of water changes with different ϵ values of the van der Waals interaction. This trend suggests that stronger attractive forces (higher ϵ) lead to a more compact arrangement of water molecules, reducing the overall volume and thus increasing the density. There is a decrease in the diffusion coefficient as ϵ increases. This trend indicates that as the attractive forces between molecules strengthen (more negative ϵ), the mobility of the molecules increases. This might seem counter-intuitive at first, as one might expect stronger attractions to slow down movement. However, this could be explained that decreasing ϵ does not only affect the attractive part of the potential but as well as the repulsive. The repulsive part of the potential becomes significant at very short distances. It's possible that with more negative ϵ, while the attraction increases, the effect on the repulsive part of the potential also becomes more pronounced. This enhanced repulsion at close distances

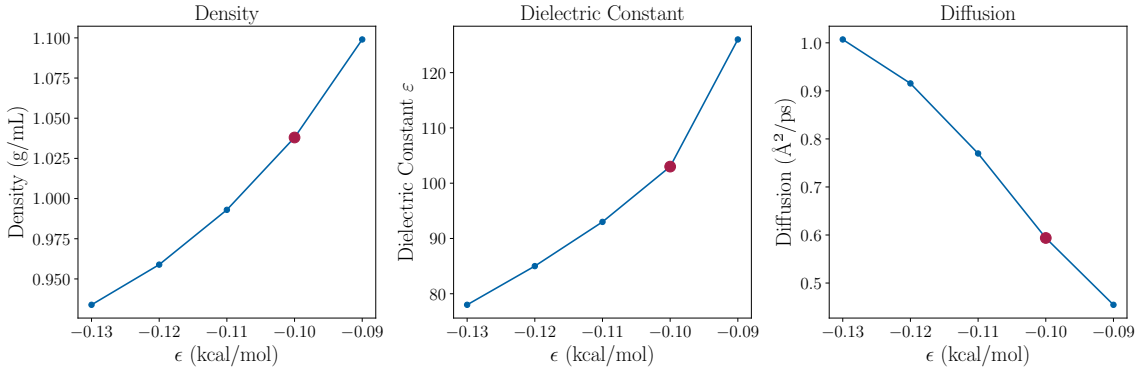

Figure 4.8.: The three figures show the effect of changing the epsilon value of the Van der Waals interactions on the density, the dielectric constant and on the diffusion of water.

could counteract the increased attraction, leading to an overall increase in molecular mobility. In simpler terms, as molecules attract each other more strongly, they also repel each other more strongly when they get too close. This dynamic could lead to an increase in the movement or diffusion of molecules, as they are constantly being pushed away from each other after reaching a certain proximity.

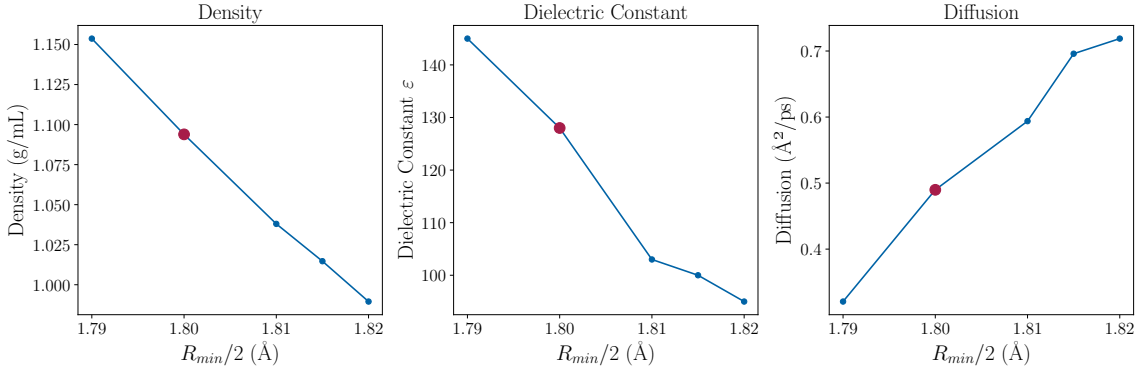

Figure 4.9.: The three figures show the effect of changing the $R_{min}/2$ value of the van der Waals interactions on the density, the dielectric constant and on the diffusion of water.

In Figure 4.9 it can be seen how $R_{min}/2$ which is directly correlated to the σ of the van der Waals interactions (see Eq. 2.21), influences the density, the dielectric constant and the diffusion of the water. The higher the σ the sooner the repulsive part of the interactions start, thus the "bigger" the molecules get. With larger oxygen atoms, the water molecules occupy more space. This reduces the number of water molecules that can fit into a given volume, leading to a decrease in density. Larger oxygen atoms might hinder the movement of water molecules, potentially reducing the diffusion rate. However,

the actual impact on diffusion could also depend on changes in molecular interactions caused by the altered size of the oxygen atoms.

The desired density of the water model should be around 1 g/mL at room temperature[94], the diffusion coefficient should be 0.23 $Å^2/ps$[95] and the dielectric constant of water is ca. 80.[96] This is best given when using the angle force constant of 500 kcal/mol·rad^2, the Drude charge of 1.08 e, the ϵ of -0.10 kcal/mol and the $R_{min}/2$ of 1.81 Å. The new water model is referred to as Drude Reactive Ionizable Polarizable Water (DRIP). A snapshot of DRIP water is shown in Figure 4.10. The model has four hydrogen atoms, out of which

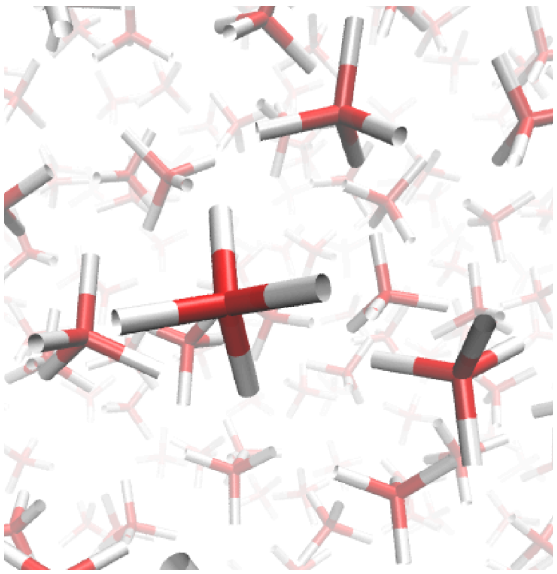

Figure 4.10.: Snapshot of DRIP water molecules, which has a tetrahedral geometry as sketched in Figure 4.5. Please note that the white sticks does not necessarily denote a hydrogen. Some of them are dummy atoms.

two are dummy hydrogens, with the same mass as the real hydrogen atoms. The dummy atoms can be switched on to create oxonium ions, or one of the real hydrogens can be switched off to make hydroxide ions. The angle between the hydrogens are 109.45°. The DRIP model shows a dielectric constant of approximately 100, notably higher than the experimental value for water, which is around 80.[96] This suggests a greater polarization response in the DRIP model compared to bulk water. The density of DRIP is 1.038 g/mL, about 4% higher than the bulk water density of 1 g/mL. The diffusion coefficient for DRIP is 0.598 $Å^2/ps$, bigger than the experimental value of 0.23 $Å^2/ps$ for bulk water. DRIP has an average dipole moment of 2.3 D (see Figure 4.11), which is compared to the experimental value 2.9 ± 0.6 D[97] is lower. All the other force field parameters can be seen in Appendix A.1.

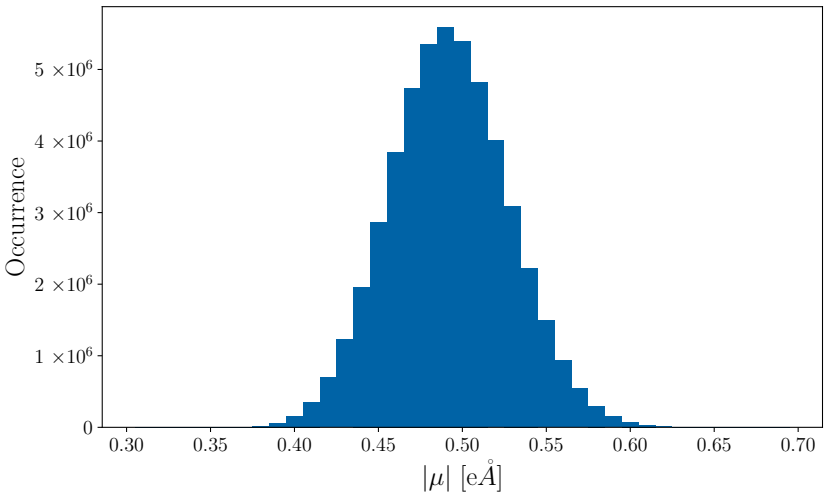

Figure 4.11.: Distribution of dipole moments of the DRIP water model sampled from an MD trajectory.

4.2.4. Comparison to common (non-)polarizable water models

Figure 4.12 shows the $g^{000}(R)$ RDF function of DRIP water model compared to SPC/E and the SWM4 water model. The first peak in the RDF corresponds to the nearest-neighbor oxygen-oxygen distance, typically reflecting the hydrogen bond network in water. The lower first peak in the DRIP model suggests that the nearest oxygen atoms are, on average, less densely packed or less strongly hydrogen-bonded compared to the SPC/E and SWM4 model. This could be due to the additional flexibility or different interaction dynamics introduced by the polarizability and the extra hydrogens in DRIP or due to the tetrahedral geometry. The deeper valley following the first peak in the SPC/E model indicates a more pronounced exclusion zone where fewer oxygen atoms are found. This is characteristic of a more structured hydrogen bond network, where water molecules are more regularly spaced due to stronger or more directional hydrogen bonding, as compared to the DRIP model. A more prominent second peak in the RDF of the SPC/E model as well as the SWM4 model suggests a more ordered arrangement of next-nearest neighbor oxygen atoms. This implies a more rigid or well-defined hydrogen bond network in the SPC/E and SWM4 model, as opposed to the DRIP model where this structure might be more relaxed or dynamic. The $g^{110}(R)$ for the DRIP, SPC/E, and SWM4 water models are illustrated in Figure 4.13. Notably, the first peaks of the RDFs for all three models exhibit similar heights, suggesting a comparable orientation of water molecules in the immediate vicinity of a reference water molecule across these models. Specifically, this similarity points to a parallel alignment of dipole moments in the first shell surrounding a water molecule. In contrast, the second peak is more pronounced in the DRIP model compared to the SPC/E and SWM4 models. This more pronounced second peak in the

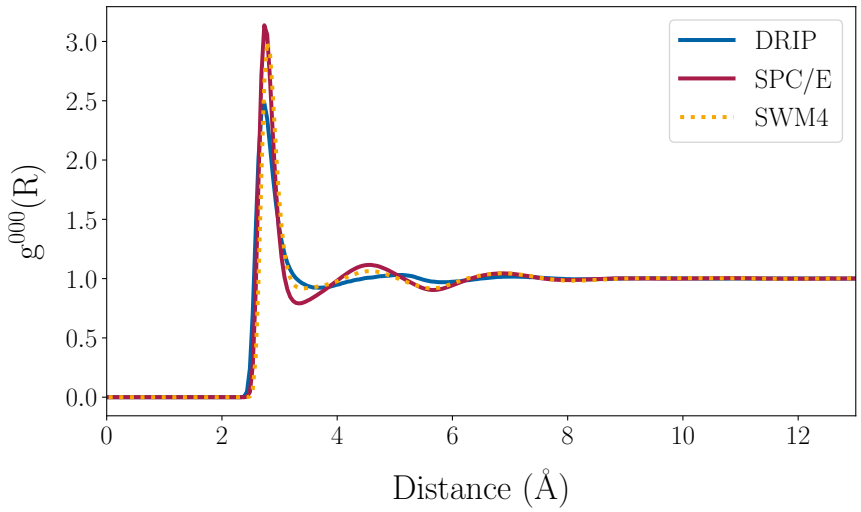

Figure 4.12.: $g^{000}(R)$ RDF function of DRIP water (blue) compared to SPC/E water model (red) and to the SWM4 water (dotted gold).

DRIP model suggests a more rigid or structured arrangement in the local environment beyond the immediate proximity of the water molecule, differing from the other two models. This difference in structure could potentially have a significant impact on the water model's dielectric constant.

The dielectric spectra of DRIP, SWM4 and SPC/E water models and of pure water can be seen in Figure 4.14. For the DRIP the dielectric constant is a little higher than 100. The SPC/E water shows the smallest permittivity but very similar to the SWM4 water model. Both these water models are underestimating the experimental value of ca. 80, while the DRIP water model overestimates.

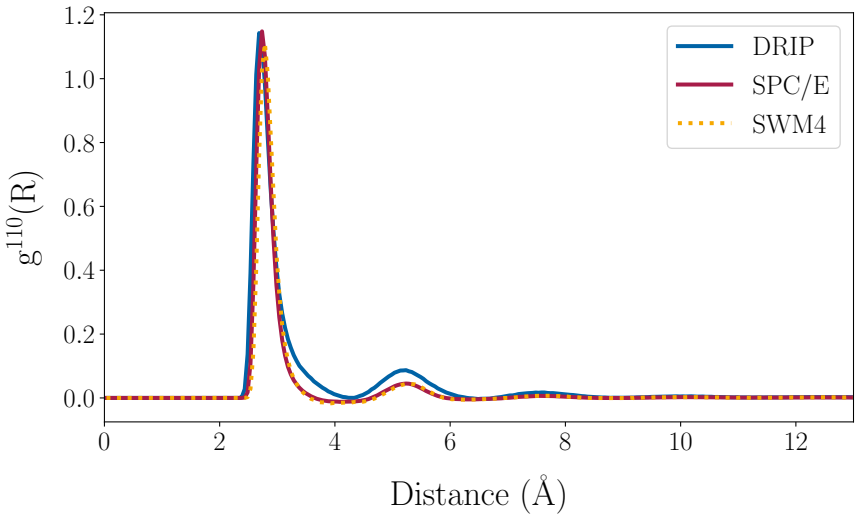

Figure 4.13.: $g^{110}(R)$ RDF function of DRIP water (blue) compared to SPC/E water model (red) and to the SWM4 water (dotted gold).

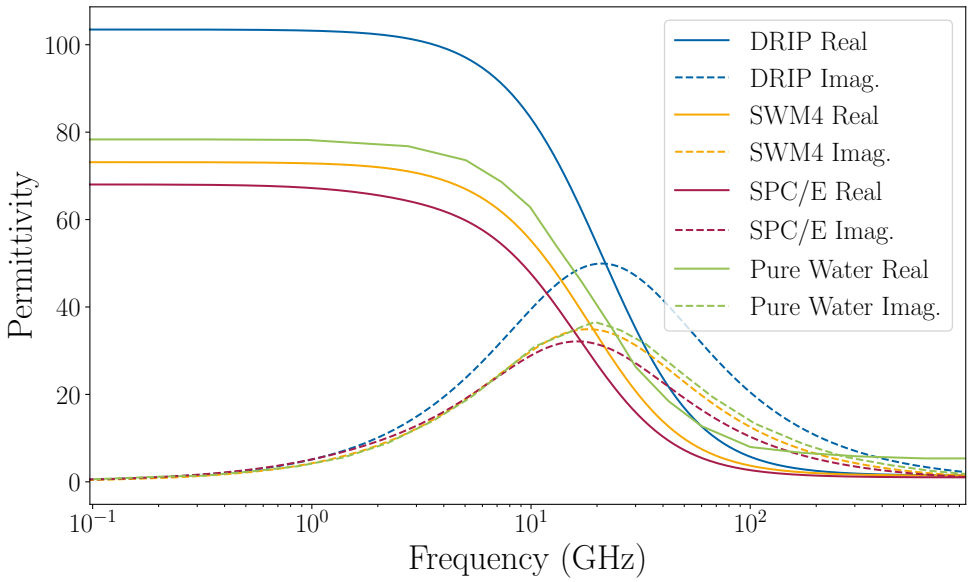

Figure 4.14.: Dielectric spectrum computed for the DRIP (blue), SWM4 (gold), SPC/E (red) water models and for pure water (green)[98]. The real part of the dielectric spectra are plotted with solid lines and the imaginary part with dotted lines.

4.3. Simulations of the M2 Channel

4.3.1. Choosing of PDB Structures and Membrane

To find the correct PDB structure for the channel, multiple PDB files were tried out like 3LBW[3,12–14,99], 1NYJ[100] and 2H95.[100] To determine the correct structure, the root mean square deviation (RMSD) from the reference structure is analyzed according to Eq. 2.29. In Figure 4.15 one can see the RMSD of these three structures embedded in POPC[9,10,12,77,99–103]membrane. As one can see the 3LBW structure stayed the most stable for 500 ns. The 3LBW and the 1NYJ structure was also simulated in the DMPC (1,2-Dimyristoyl-sn-glycero-3-phosphocholine)[13,79,102,104] membrane. It can be seen in Figure 4.16 that the 3LBW structure is more stable in the DMPC membrane as well. Since the literature uses the POPC membrane more, this lipid bilayer was chosen for further simulations.

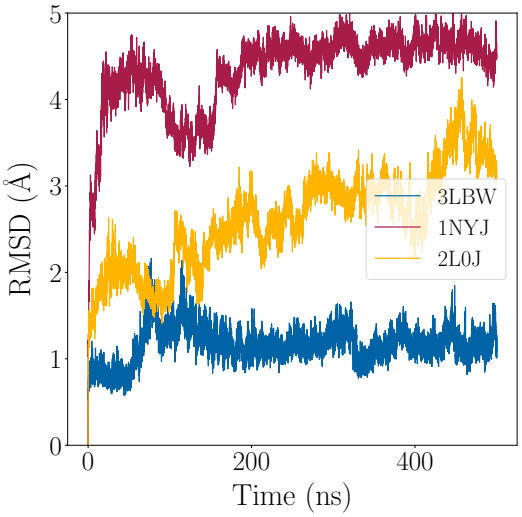

Figure 4.15.: RMSD plots of the 3LBW, 2L0J and 1NYJ PDB structures in POPC membrane.

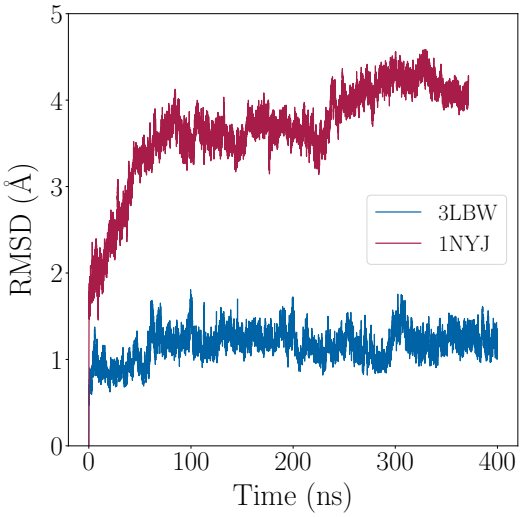

Figure 4.16.: RMSD plots of 3LBW and 1NYJ PDB structure in DMPC membrane.

4.3.2. Analyzing the Channel with Different Protonation States

In this section, different protonation states of the M2 channel are simulated. The protonation state 0 means that out of the four His37 residues all of them are HSD and not HSP residues. Protonation state +1,+2,+3 and +4 indicates then every additional HSP residue. Consistent with both experimental observations and previous computational studies, our findings indicate a direct correlation between increased protonation and channel opening (see Figure 4.17). Specifically, in the +3 and protonation state +4, the protein predominantly adopts an open conformation, while lower protonation states are associated with a closed conformation. The observed trend wherein higher protonation leads to channel opening aligns well with the increased overall RMSD of the protein under these conditions. Higher RMSD values denote significant changes from the initial PDB code structure and are thus indicating a channel opening. The protonation of His37 residues induces structural changes that facilitate the transition from a closed to an open state. Interestingly, despite the increased overall mobility of the protein with higher protonation states, the RMSD analysis of individual helices revealed their stability across all protonation states (see Figure 4.18). This observation holds true even in higher protonation states where the overall protein RMSD is substantially higher. This finding indicates that the enhanced mobility due to increased protonation does not significantly compromise the structural integrity of the individual helices. Instead, the observed increase in protein dynamics is primarily driven by changes in the interactions and relative positioning of the helices, rather than by alterations in their individual structures. The fact that individual helices show relatively low RMSD across all protonation states, even when the overall protein RMSD is high, implies that the channel opening is primarily driven by the reorientation or rearrangement of the helices relative to each other, rather

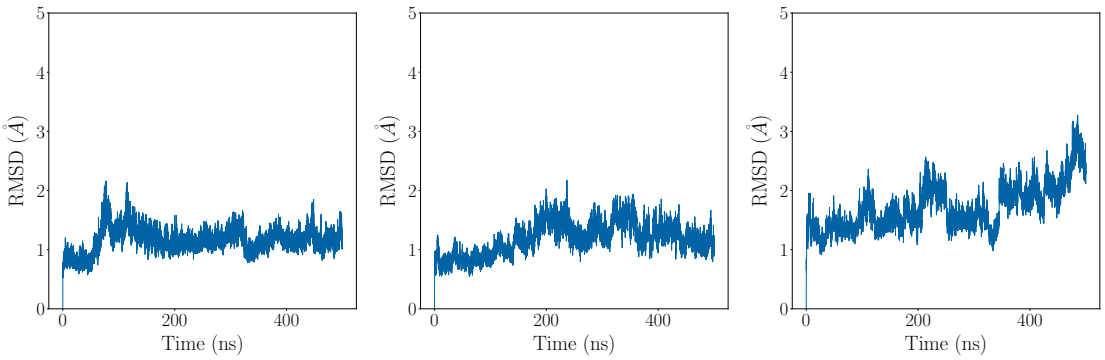

(a) Protonation state 0 (b) Protonation state +1 (c) Protonation state +2

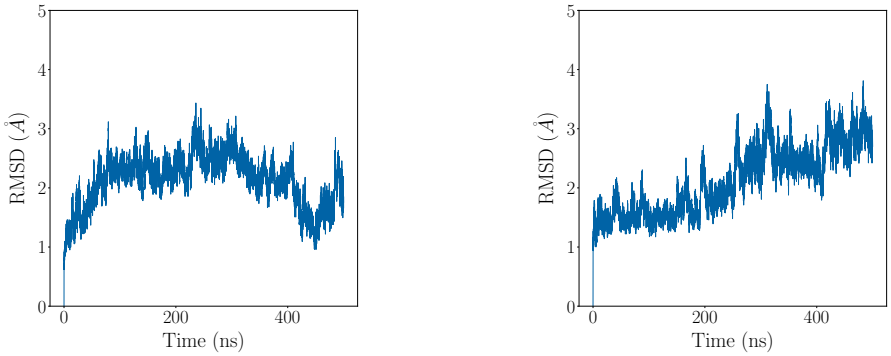

(d) Protonation state +3 (e) Protonation state +4

Figure 4.17.: RMSD of the 3LBW structure simulated in POPC membrane with five different protonation states of the His37 residues.

than significant conformational changes within the helices themselves.

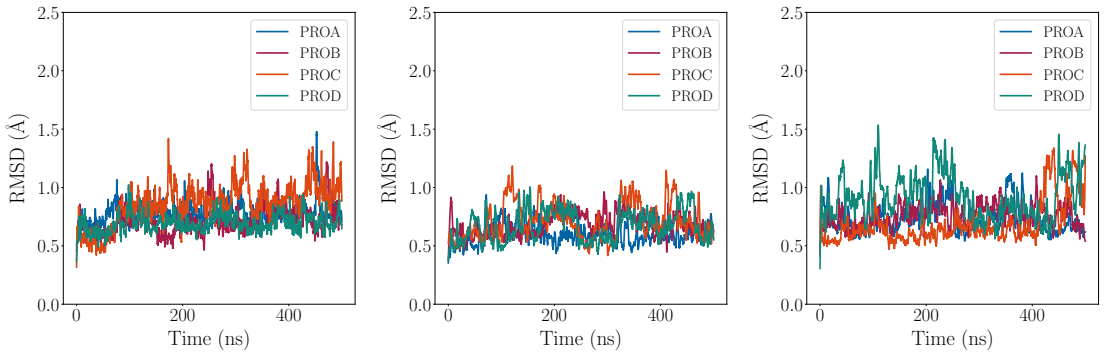

(a) Protonation state 0 (b) Protonation state +1 (c) Protonation state +2

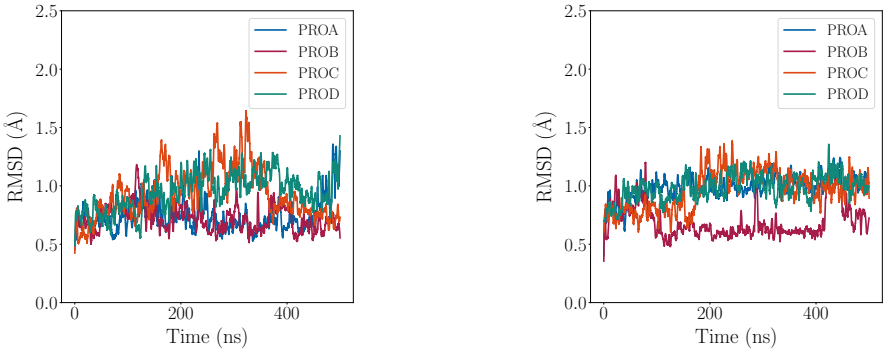

(d) Protonation state +3 (e) Protonation state +4

Figure 4.18.: RMSD of the individual helices of the 3LBW structure simulated in POPC membrane with five different protonation states of the His17 residues. PROA is depicted with blue colors, PROB with red, PROC with orange and PROD with green. The RMSD curves were smoothed with Savitzky-Golay filter.

4.3.3. Polarized Simulations with Different Protonation States

The M2 channel was also simulated with SWM4 polarizable water. In this simulation, the protein and the water are polarizable, and the membrane is not, to save computational costs. During the simulation after every 10 ns the protonation state of the channel was increased which can be seen in Figure 4.19. Even simulating with polarizable force fields the RMSD increases with every subsequent protonation step. As discussed above when the channel is more open it has higher RMSD values, which is also shown in this simulation.

Considering the charge increase during the simulation, originally dummy Cl^- ions were added which do not have a charge. In the step when a HSD residue was changed to a HSP residue, also a dummy chlorine atom was replaced by a real Cl^- one.

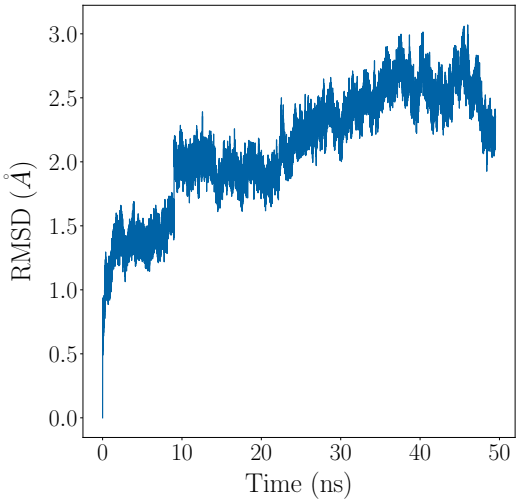

Figure 4.19.: RMSD of the channel with polarizable channel and SWM4 water model.

4.3.4. Polarized Simulations with new DRIP Water Model

In this section the newly developed DRIP water model was used in the M2 channel simulations. In these simulations oxonium ions are added in order to simulate proton transfer reactions with `protex`. The protein and the water are polarizable, but the membrane is left non-polarizable to save computational costs. First the simulation was done with four protonated His37 residues (HSP). In this production run, after 50 ns three Cl^- ions are in the channel around the positively charged HSP residues, which is depicted in Figure 4.20 (a). Due to this event, the amount of water molecules in the channel is drastically reduced to an average of nine water molecules in the channel. To investigate if the Cl^- ions are always in the channel blocking the way of the water molecules, another run of the same simulation was done. In the second run only one Cl^- ion is in the channel, which means that it is only a coincidence to have in the first simulation three ions blocking the channel (see Figure 4.20 (b)).

Looking at the RMSD values of the protein in the first run (see Figure 4.21) it can be seen that in the beginning of the simulation around 5 ns the RMSD reaches a maximum. After that it decreases again to values around 2.5-3 Å and then stays constant. The RMSD of the individual helices show that all four helices experience larger RMSD compared to the non-polarizable simulations. PROA and PROD experience more movement than PROB and PROC. In the second simulation with four protonated histidine residues the

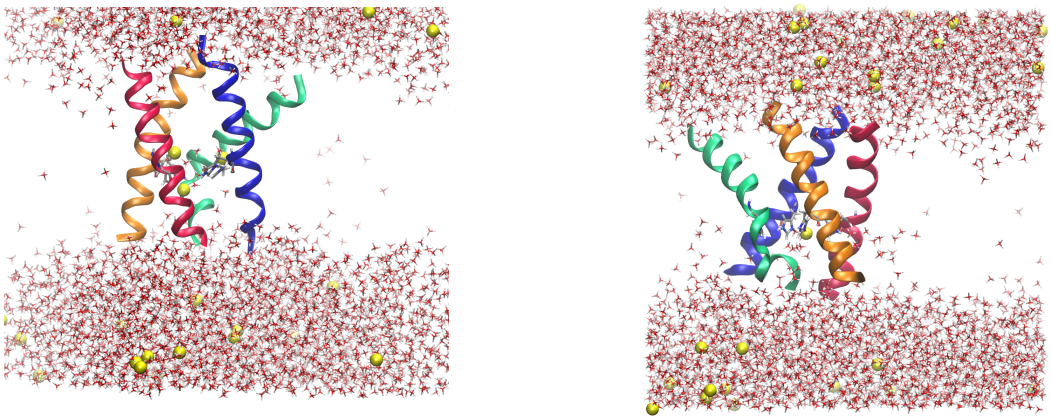

(a) (b)

Figure 4.20.: First and second simulation of the M2 channel with four HSP residues. The Cl^- ions are represented as yellow spheres. The membrane is not shown. (a) Three Cl^- ions trapped in the channel. (b) One Cl^- ion in the channel.

overall RMSD of the protein shows larger fluctuation in the RMSD compared to the first run (see Figure 4.22). The PROD helix still experiences the biggest movements among the four helices, but in the second simulation rather PROC has larger RMSD than PROA in contrast to the first simulation.

Protonation state +3 shows some large movements in the beginning of the simulation but then the whole protein stays constant (see Figure 4.23). Observing the helices the PROC helix has a larger motion than the other helices. Figure 4.24(a) shows how one Cl^- ion is trapped in the channel and in this way blocking the channel for the water molecules. It can also be seen in Figure 4.24 (b) how the membrane experiences a deformation and because of this the flow of the water molecules through the channel is hindered. This could be due to the new water model, since with the TIP3 water the membrane always stayed intact.

For protonation state +2 two simulations were run. In the first run, the two protonated HSP residues are opposite of each other, like in Figure 4.25, i.e. PROB and PROD have HSP residues and PROA and PROC have HSD residues. Looking at the RMSD of the whole protein it can be observed that in general it moves more than in the other simulations with different protonation states. However, the individual helices have no significant movements. In this case the two positively charged HSP residues are diagonally located which means they do no experience strong electrostatic repulsion due to the increased distance.

In contrast, when the two neighbouring helices are protonated (see Figure 4.26), the whole protein stays stable, while the helices PROB and PROA experience large individual movements. Since PROA and PROB have positively charged HSP residues and experience

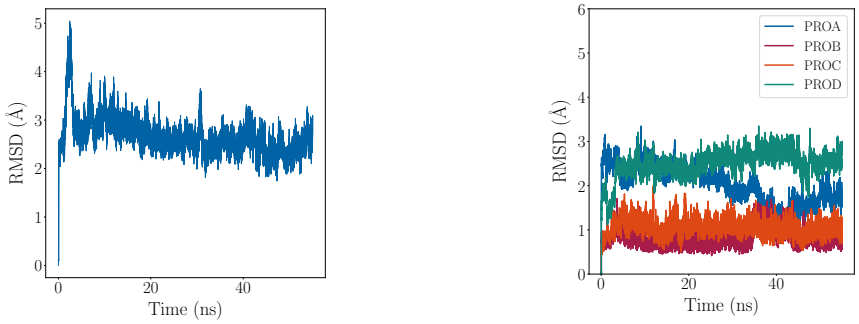

(a) (b)

Figure 4.21.: First simulation of the protonation state +4. (a) The RMSD of the whole protein. (b) The RMSD values of the individual helices. All helices have HSP residues. The RMSD curves of the individual helices were smoothed with Savitzky-Golay filter.

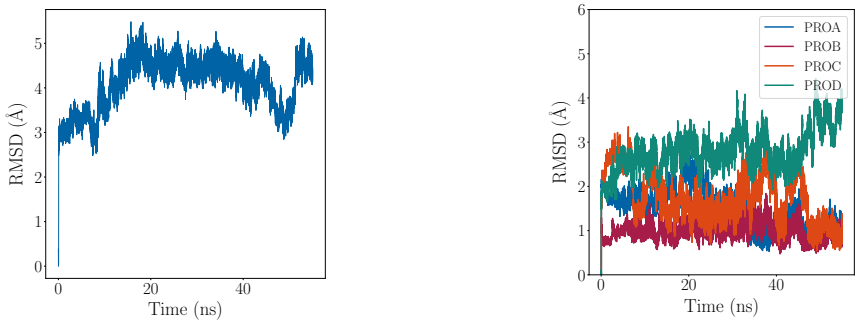

(a) (b)

Figure 4.22.: Second simulation of the protonation state +4. (a) The RMSD of the whole protein. (b) The RMSD values of the individual helices. All helices have HSP residues. The RMSD curves of the individual helices were smoothed with Savitzky-Golay filter.

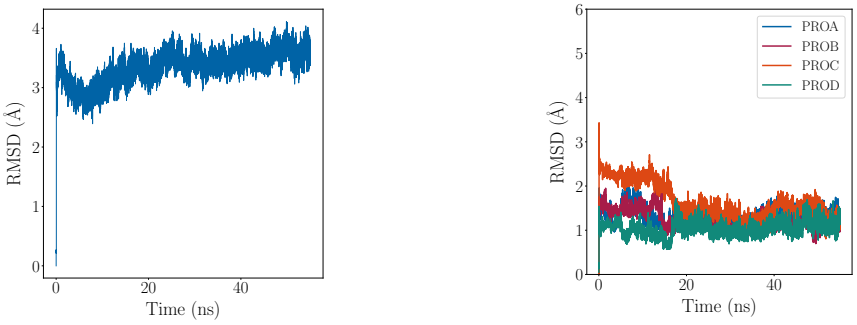

(a) (b)

Figure 4.23.: Protonation state +3 (a) The RMSD of the whole protein. (b) The RMSD values of the helices individually. All helices have HSP residues except PROD which has a HSD. The RMSD curves of the individual helices were smoothed with Savitzky-Golay filter.

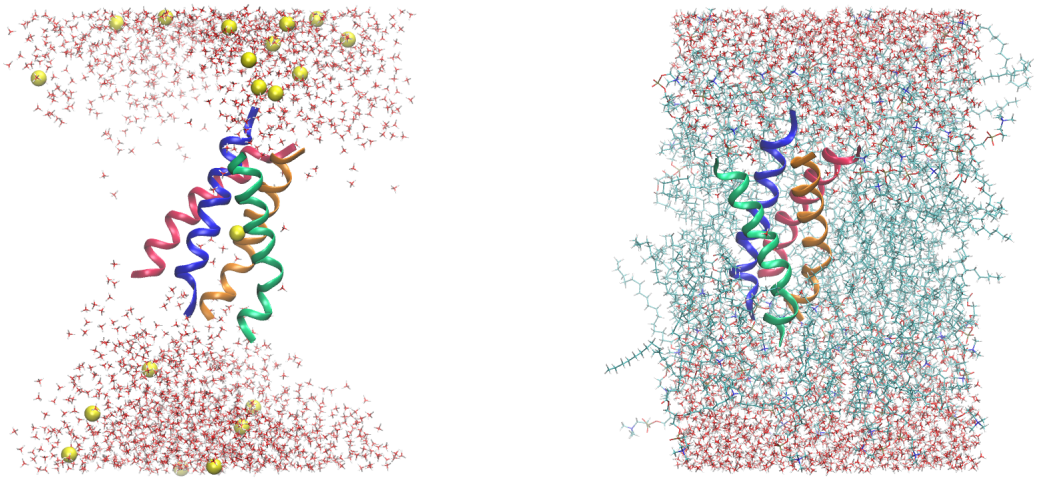

(a) (b)

Figure 4.24.: Snapshot of the simulation with protonation state +3. (a) The Cl^- ion trapped in the channel. (b) The deformation of the membrane.

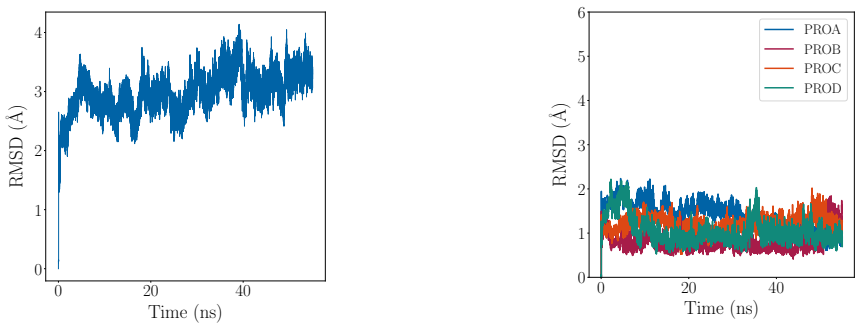

(a) (b)

Figure 4.25.: Protonation state +2 (a) The RMSD of the whole protein. (b) The RMSD values of the helices individually. PROB and PROD have HSP residues. The RMSD curves of the individual helices were smoothed with Savitzky-Golay filter.

electrostatic repulsion they find an optimal structure further apart from each other. In Figure 4.27 it can be seen again one of the complications with the new water model. The membrane deforms and the protein in the membrane is tilted. This results only in a few water molecules in the channel.

In Figure 4.28 it can be seen that the whole protein experiences notable movements. The individual helices do not move show large movements, except PROD. Figure 4.29 shows that in this simulation the membrane deforms as well as in the simulations with protonation states +2 and +3. Figure 4.30 shows the RMSD of the simulation without HSP residues. It can be seen in the RMSD that the whole protein experiences a large movement compared to the reference geometry in the beginning of the simulation with RMSD changes of ca. 4 Å. After this initial pronounced movement, the RMSD stays rather constant throughout the remaining simulation. The PROC helix shows large movements which is different comparing to the nonpolarized simulations. This is an unusual behavior since there is no electrostatic repulsion in the channel as there are no HSP residues present in this simulation. In Figure 4.31 one can see a snapshot from this simulation to understand the unusual movement of the PROC helix. As can be seen, the protein has denatured. Specifically, while the upper part of the PROC has kept the initial structure, the lower part has lost its helicity. This could explain why the RMSD shows large changes in the beginning of the simulation. However an explanation for the denaturation is not known.

Lastly, the volume of the channel with MOLE Voronoi-based program[89,90] was analyzed in simulations with different protonation states (see Figure 4.32). There, it can be seen the volume of the channel decreases with decreasing protonation states. These results are consistent with observations from the literature as summarized in the Section 1. The

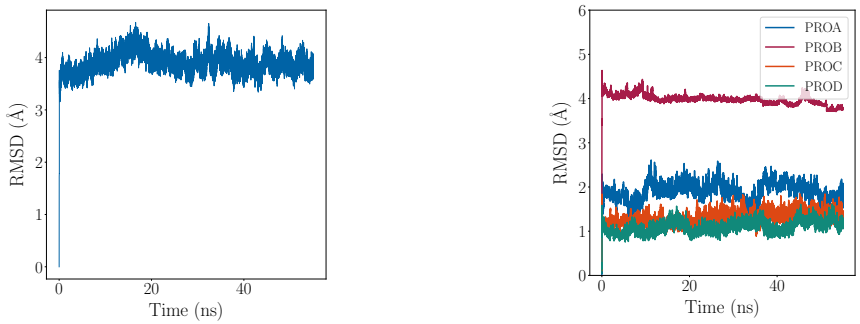

(a) (b)

Figure 4.26.: Protonation state +2 (a) The RMSD of the whole protein. (b) The RMSD values of the helices individually. PROC and PROD have HSP residues. The RMSD curves of the individual helices were smoothed with Savitzky-Golay filter.

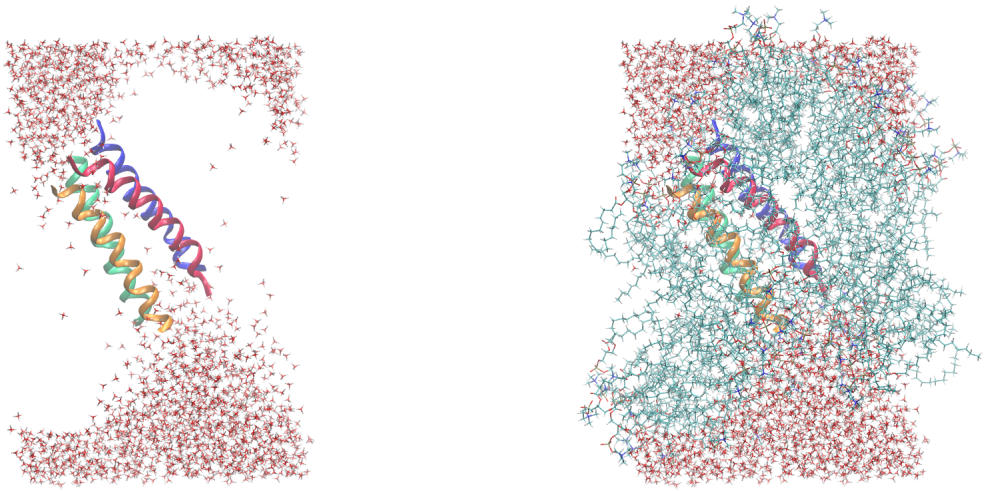

(a) (b)

Figure 4.27.: Snapshots of the simulation with protonation state +2.(a) Showing the tilted channel without the membrane. (b) Showing the deformation of the membrane.

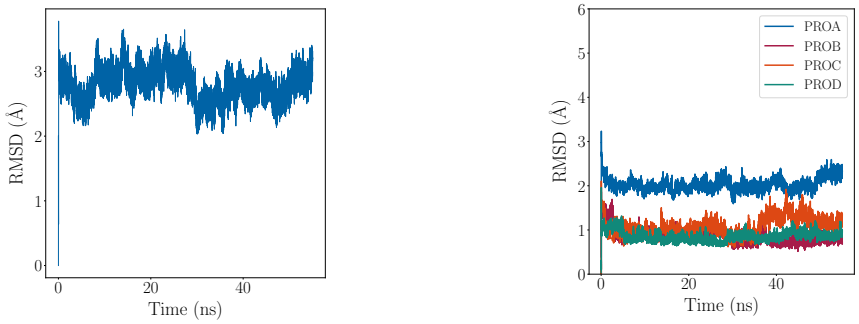

(a) (b)

Figure 4.28.: Protonation state +1 (a) The RMSD of the whole protein. (b) The RMSD values of the helices individually. PROD has a HSD residue. The RMSD curves of the individual helices were smoothed with Savitzky-Golay filter.

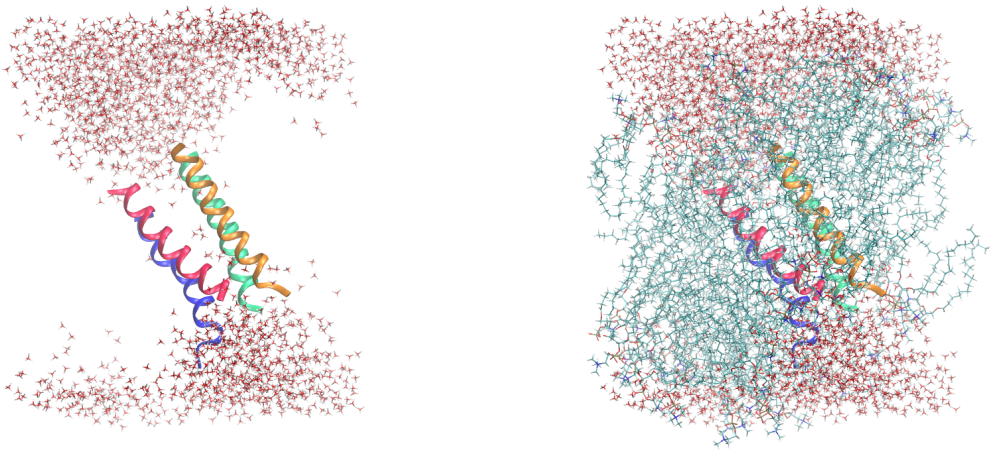

(a) (b)

Figure 4.29.: Snapshots of the simulation with protonation state +1.(a) Showing the tilted channel without the membrane. (b) Showing the deformation of the membrane.

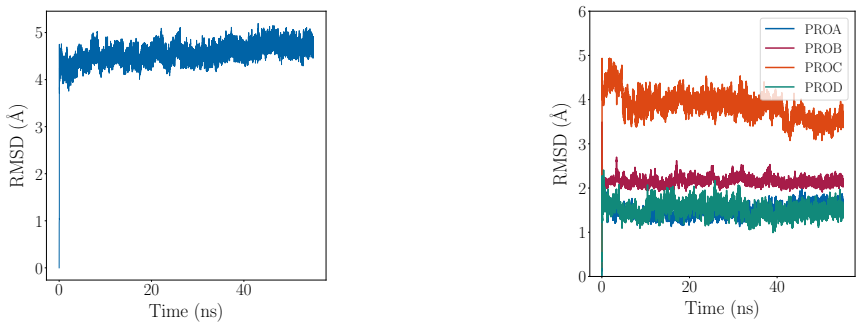

(a) (b)

Figure 4.30.: Protonation state 0 (a) The RMSD of the whole protein. (b) The RMSD values of the helices individually. All helices have HSD residues. The RMSD curves of the individual helices were smoothed with Savitzky-Golay filter.

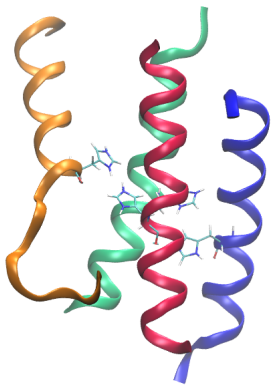

Figure 4.31.: Snapshot from the simulation without HSP residues. The membrane and the water are not shown. The orange helix represents PROC helix. The HSD residues are explicitly shown.

MOLE program can also analyze the thickness of the channel. Unfortunately, the data from these analyses cannot be transferred and replotted; therefore, this analysis is only shown for one of the protonation states, specifically state 0. The channels and their thickness, defined at every residue, can be seen in Figure 4.33. It can be observed that the convergence point of the two channels coincides with the location of the His37 residues.

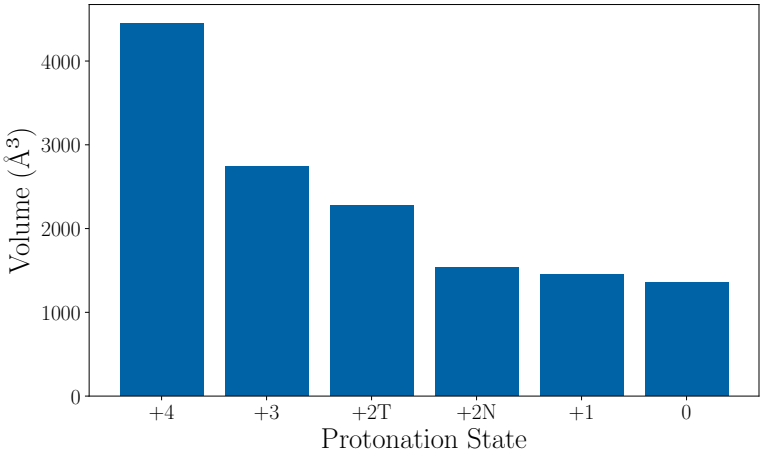

Figure 4.32.: The channel size of the different protonation states determined via MOLE software.[89,90] +2N denotes the neighbouring two HSP residues and +2T is the diagonally located two HSP residues.

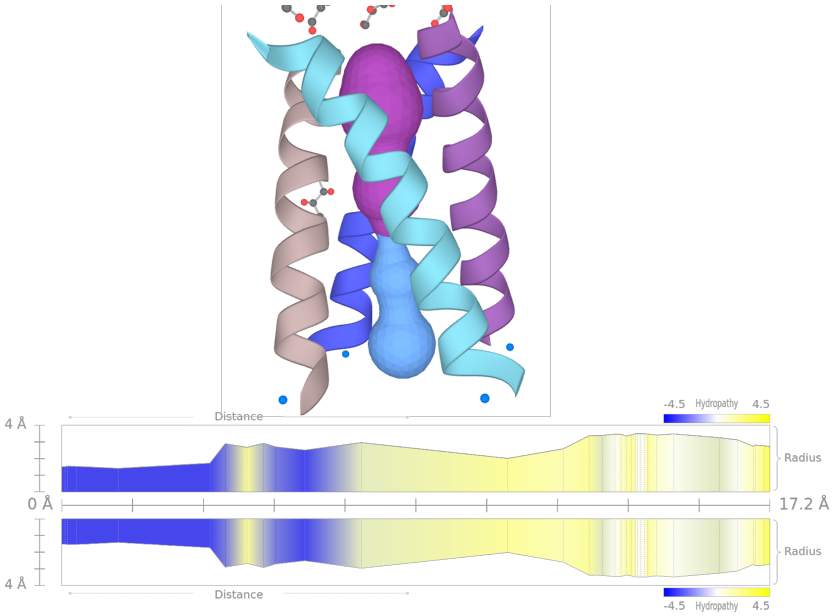

Figure 4.33.: Channels found with the MOLE program. The program has found two channels, one is depicted in purple and the other in light blue. Under the channel the thickness of the channel is depicted and colored according to the hydropathy of the residues.

5. Conclusion

This work aimed to simulate the M2 channel of the Influenza A virus using a reactive water model within the `protex` framework. To do this, first quantum mechanical (QM) scans to establish reaction probabilities were simulated, a critical step for accurate modeling in `protex`. As a next step a new water model was developed capable to describe multiple protonation states. Using this water model the dynamics of the channel was simulated with different protonation states. As a last step, `protex` was planned to be used to model the complete proton transfer mechanism through the channel. `protex` requires further development, which was unfortunately not completed during this work. Instead the focus of this work was shifted towards the conformational dynamics of the channel under various protonation states without direct observation of proton transfer processes.

While performing the QM scans it was found that accurately simulating proton transfer in water does not work only using two or four explicit water molecules due to the incomplete stabilization with hydrogen bonds. Instead to obtain a realistic description at least six water molecules should be explicitly simulated.

Second part of the work was the development of the Drude Reactive Ionizable Polarizable Water (DRIP) model. This was done by systematic alterations to force field parameters, specifically targeting the optimization of macroscopic properties such as density, diffusion, and dielectric constant of water. These modifications were essential in ensuring that the DRIP model accurately reflected the physical properties of water, thereby enhancing the realism and relevance of the simulations.

Furthermore the work involved simulating a range of PDB structures and lipid bilayer configurations to determine the most effective setup for analyzing the M2 channel under different protonation states. The simulations revealed that in the protonation state +2, the conformation of the channel is significantly influenced by the spatial arrangement of the protonated helices. When two adjacent helices were protonated, these helices exhibited larger movements due to electrostatic repulsion, highlighting the complexity of electrostatic interactions within the channel. Furthermore, it was observed that the channel adopts an open conformation when at least three His37 residues are protonated, primarily due to electrostatic repulsion between the positively charged residues.

In order to simulate the proton transfer with `protex` further development is required. In addition, future research could focus on longer simulation times up to μs time scales, to obtain an accurate description of the biochemical processes of the M2 channel. Further development of the force fields can potentially improve the accuracy of the simulations. With these adjustments a more detailed dynamics of the M2 channel could be revealed and potential residues of the channel could be targeted to inactivate the virus.

A. Appendix

A.1. Water Parametrization

For the water parametrization different parameters were tried out. In Table A.2 the different water models can be seen. While in Table A.1 in the water model only one parameter at the time was changed to obtain trends.

$R_{min}/2$	ϵ_{VdW}	FC Angle	Drude Charge	Dielectric Const.	Diffusion coeff.	Density
1.810	-0.10	50	-1.08	132	0.5798	1.0549
1.810	-0.10	100	-1.08	115	0.5786	1.0466
1.810	-0.10	200	-1.08	109	0.6351	1.0417
1.810	-0.10	500	-1.08	103	0.5938	1.0380
1.810	-0.10	1000	-1.08	107	0.6767	1.0411
1.810	-0.09	500	-1.08	126	0.4547	1.0990
1.810	-0.10	500	-1.08	103	0.5938	1.0380
1.810	-0.11	500	-1.08	93	0.7697	0.9930
1.810	-0.12	500	-1.08	85	0.9155	0.9589
1.810	-0.13	500	-1.08	78	1.007	0.9339
1.790	-0.10	500	-1.08	145	0.3206	1.1537
1.800	-0.10	500	-1.08	128	0.4898	1.0939
1.810	-0.10	500	-1.08	103	0.5938	1.0380
1.815	-0.10	500	-1.08	100	0.6959	1.0147
1.820	-0.10	500	-1.08	95	0.7188	0.9895
1.810	-0.10	500	-1.01	91	0.7893	1.0046
1.810	-0.10	500	-1.05	98	0.6787	1.0240
1.810	-0.10	500	-1.08	103	0.5938	1.0380
1.810	-0.10	500	-1.20	164	0.3464	1.1164
1.810	-0.10	500	-1.44	22	0.9230	1.5939

Table A.1.: Parameters of the water model and macroscopic properties of the bulk water obtained in the simulations.$R_{min}/2$ is in Å. ϵ_{VdW} stands for the ϵ value of the Van der Waals interactions and has a unit of kcal/mol. FC is force constant and is in kcal/molrad^2. The Drude charge is in unit charge e. The dielectric constant doe snot have a unit. The diffusion coefficient is in Å^2/ps and lastly the density has a unit of g/mL.

$R_{min}/2$	ϵ_{VdW}	FC Angle	Drude Charge	Dielectric Const.	Diffusion coeff.	Density
1.829	-0.115	200	-1.44	260	0.3736	1.073
1.829	-0.115	300	-1.44	280	0.3493	1.083
1.829	-0.115	400	-1.44	270	0.3288	1.082
1.829	-0.115	50	-1.20	140	0.8305	0.955
1.829	-0.115	50	-1.10	113	1.0847	0.910
1.829	-0.115	50	-1.05	103	1.1182	0.891
1.829	-0.115	200	-1.20	125	0.9011	0.942
1.829	-0.115	200	-1.05	93	1.1763	0.875
1.829	-0.115	50	-1.02	97	1.2348	0.878
1.829	-0.100	200	-1.02	97	0.9945	0.899
1.829	-0.100	50	-1.02	109	0.9588	0.931
1.829	-0.130	200	-1.20	115	1.0964	0.899
1.829	-0.130	50	-1.20	123	1.0662	0.910
1.829	-0.130	200	-1.02	81	1.4518	0.835
1.829	-0.130	500	-1.02	81	1.4841	0.831
1.829	-0.115	500	-1.02	88	1.2589	0.867
1.829	-0.110	500	-1.03	91	1.2311	0.886
1.829	-0.110	800	-1.02	90	1.2421	0.883
1.829	-0.110	500	-1.05	-	-	0.954
1.829	-0.100	500	-1.10	-	-	0.893
1.810	-0.13	500	-1.20	90	0.7930	0.980
1.810	-0.13	500	-1.08	62	1.01287	0.932
1.810	-0.09	500	-1.08	140	0.4345	1.0986
1.815	-0.09	500	-1.08	120	0.5085	1.068
1.800	-0.110	500	-1.08	105	0.6060	1.056
1.810	-0.110	500	-1.08	85	0.7539	0.995
1.800	-0.13	500	-1.20	117	0.6574	1.028
1.810	-0.10	500	-1.20	-	-	-
1.810	-0.10	500	-1.08	103	0.5938	1.038

Table A.2.: Parameters of the water model and macroscopic properties of the bulk water obtained in the simulations.$R_{min}/2$ is in Å. ϵ_{VdW} stands for the ϵ value of the Van der Waals interactions and has a unit of kcal/mol. FC is force constant and is in kcal/molrad^2. The Drude charge is in unit charge e. The dielectric constant doe snot have a unit. The diffusion coefficient is in Å^2/ps and lastly the density has a unit of g/mL.

The following force-field parameters are for the DRIP water, which is called a TOH2 residue:

```
ioformat extended
```

```
read rtf card ! append
44

MASS    1 HPOL      1.00800 H  ! IPOL13 and IPOL16 water H
MASS    2 OPOL13   15.99940 O  ! IPOL13 water oxygen
MASS    3 DRUD      0.00000 H  ! IPOL water oxygen drude particle
MASS    4 DUMH      1.00800 H  ! dummy H

DEFA FIRST NONE LAST NONE
AUTOGENERATE ANGLES DIHEDRALS PATCH DRUDE

RESI TOH2          0.000 !
GROUP
ATOM OH2  OPOL13     -0.669    ALPHA -1.08 THOLE 1.3
ATOM H1   HPOL      0.3345
ATOM H2   HPOL      0.3345
ATOM H3   DUMH     0.000
ATOM H4   DUMH     0.000
BOND OH2 H1
BOND OH2 H2
BOND OH2 H3
BOND OH2 H4
ANGLE  H1 OH2 H2
ANGLE  H1 OH2 H3
ANGLE  H3 OH2 H2
ANGLE  H1 OH2 H4
ANGLE  H2 OH2 H4
ANGLE  H3 OH2 H4

PATCH FIRST NONE LAST NONE

END

read param card ! append
BONDS
OPOL13   HPOL     450.00      0.9619 ! IPOL13 water
OPOL13   DUMH     450.00      0.9619 ! TETRA water
X        DRUD    1000.00      0.000 !

ANGLES
HPOL     OPOL13   HPOL     500.000   109.47 ! TETRA water
HPOL     OPOL13   DUMH     500.000   109.47 ! TETRA water
DUMH     OPOL13   DUMH     500.000   109.47 ! TETRA water
```

```
DIHEDRALS

IMPROPERS

CMAP

NONBONDED nbxmod  5 atom vatom cdiel vdistance switch vswitch -
cutnb 16.0 ctofnb 12.0 ctonnb 10.0 eps 1.0 e14fac 1.0 wmin 1.5

OPOL13  0.00   -0.100      1.8100 ! IPOL13
HPOL    0.00   -0.000      0.0000  ! IPOL13
DUMH    0.00   -0.000      0.0000  ! IPOL13
DRUD    0.00   -0.000      0.0100 ! Generic Drudes

END
```

A.2. Histidine Force Fields

To make a proton transfer possible for the HSP and HSD residue, additional lone pairs, and dummy atoms were added to these residues. Here are the following changes that were made:

```
    RESI HSD           0.000 ! neutral HIS, proton on ND1
!
!      |         HD1       HE1
!  HN-N           \       /
!      |   HB1    ND1--CE1
!      |   |     /       ||
!  HA-CA--CB--CG         ||
!      |   |     \\      ||
!      |   HB2    CD2--NE2
!   O=C            |       \
!      |           HD2     DUMH
!
GROUP
ATOM N    ND2A2   -0.406  ALPHA -1.858  THOLE 0.126
ATOM HN   HDP1A    0.296
ATOM CA   CD31C    0.170  ALPHA -1.066  THOLE 1.141
ATOM HA   HDA1A   -0.017
ATOM C    CD2O1A   0.495  ALPHA -0.619  THOLE 0.317
ATOM O    OD2C1A   0.000  ALPHA -0.579  THOLE 0.370
ATOM LPOA LPDO1   -0.311
ATOM LPOB LPDO1   -0.227
```

```
GROUP
ATOM CB   CD32A   -0.019  ALPHA  -1.486  THOLE  0.427
ATOM HB1  HDA2A    0.075
ATOM HB2  HDA2A    0.075
ATOM ND1  ND2R5A  -0.057  ALPHA -1.522  THOLE 1.114
ATOM HD1  HDP1A    0.252
ATOM NE2  ND2R5B   0.000  ALPHA -1.146  THOLE 0.816
ATOM HE2  DUMH     0.000
ATOM CG   CD2R5A  -0.250  ALPHA -1.272  THOLE 1.190
ATOM CE1  CD2R5B   0.034  ALPHA -1.493  THOLE 1.297
ATOM HE1  HDR5B    0.104
ATOM CD2  CD2R5A   0.005  ALPHA -1.515  THOLE 1.190
ATOM HD2  HDR5A    0.113
ATOM LPE2 LPD     -0.332
ATOM LPA  LP5N     0.000

BOND N    CA        CA   C         C    +N        CA   HA
BOND N    HN        C    O
BOND CA   CB        CB   HB1       CB   HB2
BOND CB   CG        CG   ND1       ND1  CE1       CE1  NE2
BOND NE2  CD2       CD2  CG
BOND ND1  HD1       CE1  HE1       CD2  HD2       NE2  HE2
BOND O    LPOA      O    LPOB
BOND NE2  LPE2

IMPR ND1  CG   CE1  HD1       CD2  CG  NE2  HD2
IMPR CE1  ND1  NE2  HE1       NE2  CE1 CD2  HE2
IMPR C   CA  +N  O   N  -C  CA HN
CMAP -C  N   CA  C   N  CA  C  +N

LONEPAIR bisector LPA ND1 CG CE1 distance  1.173 angle   0.0 dihe 0.0 ! fylin
LONEPAIR relative LPOA O C CA distance 0.30 angle 91.0 dihe   0.0
LONEPAIR relative LPOB O C CA distance 0.30 angle 91.0 dihe 180.0
ANISOTROPY O C LPOA LPOB  A11  0.82322 A22  1.14332

LONEPAIR bisector LPE2 NE2 CE1 CD2  distance 0.35 angle 179.99 dihe 179.99
ANISOTROPY        NE2 LPE2 CE1 CD2  A11 0.808   A22 1.384

DONOR HN N
DONOR HD1 ND1
ACCEPTOR NE2
ACCEPTOR O C
!IC table
```

```
IC -C   CA   *N   HN    1.3475 123.2700  180.0000 115.2100  0.9988
IC -C   N    CA   C     1.3475 123.2700  180.0000 107.7000  1.5166
IC N    CA   C    +N    1.4521 107.7000  180.0000 117.5700  1.3509
IC +N   CA   *C   O     1.3509 117.5700  180.0000 120.2400  1.2273
IC CA   C    +N   +CA   1.5166 117.5700  180.0000 123.7200  1.4545
IC N    C    *CA  CB    1.4521 107.7000  122.4600 109.9900  1.5519
IC N    C    *CA  HA    1.4521 107.7000 -117.4900 107.3700  1.0830
IC N    CA   CB   CG    1.4521 112.1200  180.0000 114.0500  1.5041
IC CG   CA   *CB  HB1   1.5041 114.0500  121.1700 109.0100  1.1118
IC CG   CA   *CB  HB2   1.5041 114.0500 -122.3600 109.5300  1.1121
IC CA   CB   CG   ND1   1.5519 114.0500   90.0000 124.1000  1.3783
IC ND1  CB   *CG  CD2   1.3783 124.1000 -171.2900 129.6000  1.3597
IC CB   CG   ND1  CE1   1.5041 124.1000 -173.2100 107.0300  1.3549
IC CB   CG   CD2  NE2   1.5041 129.6000  171.9900 110.0300  1.3817
IC NE2  ND1  *CE1 HE1   1.3166 111.6300 -179.6300 123.8900  1.0932
IC CE1  CD2  *NE2 HE2   1.3256 108.8200 -172.9400 125.5200  1.0020
IC CE1  CG   *ND1 HD1   1.3549 107.0300 -174.6500 126.2600  1.0005
IC NE2  CG   *CD2 HD2   1.3817 110.0300 -177.8500 129.6300  1.0834


    RESI HSP           1.000 ! protonated HIS
!
!      |         HD1      HE1
!  HN-N           \       /
!      |   HB1    ND1--CE1
!      |   |     /       ||
!  HA-CA--CB--CG         ||
!      |   |     \\      ||
!      |   HB2    CD2--NE2
!   O=C             |      \
!      |           HD2     HE2
!
GROUP
ATOM N    ND2A2   -0.406  ALPHA -1.858  THOLE 0.126
ATOM HN   HDP1A    0.296
ATOM CA   CD31C    0.170  ALPHA -1.066  THOLE 1.141
ATOM HA   HDA1A   -0.017
ATOM C    CD2O1A   0.495  ALPHA -0.619  THOLE 0.317
ATOM O    OD2C1A   0.000  ALPHA -0.579  THOLE 0.370
ATOM LPOA LPDO1   -0.311
ATOM LPOB LPDO1   -0.227
GROUP
ATOM CB   CD32A    0.017  ALPHA  -0.451  THOLE  0.419
ATOM HB1  HDA2A    0.078 !from HSD/HSE
```

```
ATOM HB2  HDA2A    0.078 !from HSD/HSE
ATOM ND1  ND2R5C  -0.171  ALPHA -1.260  THOLE 1.194
ATOM HD1  HDP1A    0.340
ATOM NE2  ND2R5C  -0.171  ALPHA -1.260  THOLE 1.194
ATOM HE2  HDP1A    0.340
ATOM CG   CD2R5D  -0.012  ALPHA -1.522  THOLE 1.196
ATOM CE1  CD2R5E   0.170  ALPHA -1.500  THOLE 1.317
ATOM HE1  HDR5E    0.170
ATOM CD2  CD2R5D  -0.012  ALPHA -1.522  THOLE 1.196
ATOM HD2  HDR5D    0.173
ATOM LPE2 LPD     -0.000
ATOM LPA  LP5N     0.000

BOND N    CA        CA   C         C    +N        CA   HA
BOND N    HN        C    O
BOND CA   CB        CB   HB1       CB   HB2
BOND CB   CG        CG   ND1       ND1  CE1       CE1  NE2
BOND NE2  CD2       CD2  CG
BOND ND1  HD1       CE1  HE1       CD2  HD2       NE2  HE2
BOND O    LPOA      O    LPOB
BOND NE2  LPE2


IMPR ND1  CE1  CG   HD1       NE2  CE1 CD2  HE2
IMPR CE1  ND1  NE2  HE1       CD2  CG  NE2  HD2
IMPR C   CA  +N  O   N  -C  CA HN
CMAP -C  N   CA  C   N  CA  C  +N

LONEPAIR bisector LPA ND1 CG CE1 distance  1.173 angle   0.0 dihe 0.0 ! fylin
LONEPAIR relative LPOA O C CA distance 0.30 angle 91.0 dihe   0.0
LONEPAIR relative LPOB O C CA distance 0.30 angle 91.0 dihe 180.0
ANISOTROPY O C LPOA LPOB  A11  0.82322 A22  1.14332

LONEPAIR bisector LPE2 NE2 CE1 CD2  distance 0.35 angle 179.99 dihe 179.99
ANISOTROPY        NE2 LPE2 CE1 CD2  A11 0.808   A22 1.384

DONOR HN N
DONOR HD1 ND1
DONOR HE2 NE2
ACCEPTOR O C
!IC table
IC -C   CA   *N   HN    1.3489 123.9300  180.0000 118.8000  1.0041
IC -C   N    CA   C     1.3489 123.9300  180.0000 112.0300  1.5225
```

```
IC N    CA   C    +N    1.4548 112.0300  180.0000 116.4900  1.3464
IC +N   CA   *C   O     1.3464 116.4900  180.0000 121.2000  1.2284
IC CA   C    +N   +CA   1.5225 116.4900  180.0000 124.2400  1.4521
IC N    C    *CA  CB    1.4548 112.0300  125.1300 109.3800  1.5533
IC N    C    *CA  HA    1.4548 112.0300 -119.2000 106.7200  1.0832
IC N    CA   CB   CG    1.4548 112.2500  180.0000 114.1800  1.5168
IC CG   CA   *CB  HB1   1.5168 114.1800  122.5000 108.9900  1.1116
IC CG   CA   *CB  HB2   1.5168 114.1800 -121.5100 108.9700  1.1132
IC CA   CB   CG   ND1   1.5533 114.1800   90.0000 122.9400  1.3718
IC ND1  CB   *CG  CD2   1.3718 122.9400 -165.2600 128.9300  1.3549
IC CB   CG   ND1  CE1   1.5168 122.9400 -167.6200 108.9000  1.3262
IC CB   CG   CD2  NE2   1.5168 128.9300  167.1300 106.9300  1.3727
IC NE2  ND1  *CE1 HE1   1.3256 108.5000  178.3900 125.7600  1.0799
IC CE1  CD2  *NE2 HE2   1.3256 108.8200 -172.9400 125.5200  1.0020
IC CE1  CG   *ND1 HD1   1.3262 108.9000  171.4900 126.0900  1.0018
IC NE2  CG   *CD2 HD2   1.3727 106.9300 -174.4900 128.4100  1.0867
```

A.3. Packmol Example Input File

The following Packmol input file was used to put together an OpenMM simulation including the membrane, the protein, ions and the DRIP water model:

```
tolerance 3.0
seed -1
nloop0 2000

filetype pdb
output ptoh2_init.pdb

structure pdb/ppp3.pdb # prot+membrane pdb
  number 1
  inside box -35 -35 -31 35 35 31
end structure

structure pdb/h2o.pdb
  number 2500
  inside box -35 -35 -51 35 35 51
end structure

structure pdb/h3o.pdb
  number 8
  inside box -35 -35 -51 35 35 51
end structure

structure pdb/ions.pdb
  number 1
  inside box -35 -35 -51 35 35 51
end structure

structure pdb/cl.pdb
  number 7
  inside box -35 -35 -51 35 35 51
end structure
```

B. Zusammenfassung

Das Influenza-A-Virus ist eine Hauptursache für saisonale Grippeepidemien. Das Virus ist für seine Replikation auf die Funktionalität des M2-Protonenkanals angewiesen, was ihn zu einem entscheidenden Ziel für die Entwicklung antiviraler Medikamente macht. Ziel dieser Arbeit ist es, das Verständnis dieses Kanals zu verbessern, indem sein Protonentransfer-Mechanismus mit einem reaktiven Wassermodell innerhalb der klassischen Molekulardynamik und des `protex` -Frameworks simuliert wurde. Protex ist ein Python-basiertes Werkzeug, um Protonenübertragungen zwischen Molekülen in molekulardynamischen Simulationen zu ermöglichen. Folglich werden zeitaufwändige quantenmechanische Simulationen dieser Reaktionen bis zu einem gewissen Grad überflüssig. Eine wichtige Entwicklung in dieser Forschung war die Entwicklung des Drude Reactive Ionizable Polarizable Water (DRIP)-Modells, das zur Beschreibung von Protonentransfer-Simulationen in `protex` entwickelt wurde. Simulationen wurden durchgeführt, um das Verhalten des Kanals unter verschiedenen Protonierungszuständen zu beobachten, wobei sich zeigte, dass der Kanal eine offene Konformation beibehält, wenn drei oder vier Histidinreste protoniert sind. Diese Ergebnisse stimmen mit denen aus anderen experimentellen und rechnerischen Studien überein und zeigen, dass die funktionale Dynamik des Kanals selbst mit polarisierbaren Kraftfeldern und dem neuen Wassermodell effektiv simuliert und verstanden werden kann.

Bibliography

[1] F. Hu, W. Luo, and M. Hong. Mechanisms of Proton Conduction and Gating in Influenza M2 Proton Channels from Solid-State NMR. *Science*, 330(6003):505–508, 2010.

[2] F. Hu, K. Schmidt-Rohr, and M. Hong. NMR Detection of pH-Dependent Histidine-Water Proton Exchange Reveals the Conduction Mechanism of a Transmembrane Proton Channel. *JACS*, 134(8):3703–3713, 2011.

[3] M. Hong, K. J. Fritzsching, and J. K. Williams. Hydrogen-Bonding Partner of the Proton-Conducting Histidine in the Influenza M2 Proton Channel Revealed From ^{1}H Chemical Shifts. *JACS*, 134(36):14753–14755, 2012.

[4] B. Jeong and R. B. Dyer. Proton Transport Mechanism of M2 Proton Channel Studied by Laser-Induced pH Jump. *JACS*, 139(19):6621–6628, 2017.

[5] R. Fu, Y. Miao, H. Qin, and T. A. Cross. Observation of the Imidazole-Imidazolium Hydrogen Bonds Responsible for Selective Proton Conductance in the Influenza A M2 Channel. *JACS*, 2020.

[6] W. L. Jorgensen, J. Chandrasekhar, J. D. Madura, R. W. Impey, and M. L. Klein. Comparison of Simple Potential Functions for Simulating Liquid Water. *J. Chem. Phys.*, 79:926–935, 1983.

[7] Q. Zhong, Q. Jiang, P. B. Moore, D. M. Newns, and M. L. Klein. Molecular Dynamics Simulation of a Synthetic Ion Channel. *Biophys. J.*, 74(1):3–10, 1998.

[8] E. Khurana, M. D. Peraro, R. DeVane, S. Vemparala, W. F. DeGrado, and M. L. Klein. Molecular Dynamics Calculations Suggest a Conduction Mechanism for the M2 Proton Channel from Influenza A Virus. *PNAS*, 106(4):1069–1074, 2009.

[9] V. Carnevale, G. Fiorin, B. G. Levine, W. F. DeGrado, and M. L. Klein. Multiple Proton Confinement in the M2 Channel from the Influenza A Virus. *JPCC*, 114(48):20856–20863, 2010.

[10] C. Wei and A. Pohorille. Activation and Proton Transport Mechanism in Influenza A M2 Channel. *Biophys. J.*, 105(9):2036–2045, 2013.

[11] H. Dong, G. Fiorin, W. F. DeGrado, and M. L. Klein. Exploring Histidine Conformations in the M2 Channel Lumen of the Influenza A Virus at Neutral pH via Molecular Simulations. *JPCL*, 4(18):3067–3071, 2013.

[12] H. Dong, G. Fiorin, W. F. DeGrado, and M. L. Klein. Proton Release from the Histidine-Tetrad in the M2 Channel of the Influenza A Virus. *JPCB*, 118(44):12644–12651, 2014.

[13] W. Chen, Y. Huang, and J. Shen. Conformational Activation of a Transmembrane Proton Channel from Constant pH Molecular Dynamics. *JPCL*, 7(19):3961–3966, 2016.

[14] R. Liang, H. Li, J. M. J. Swanson, and G. A. Voth. Multiscale Simulation Reveals a Multifaceted Mechanism of Proton Permeation Through the Influenza A M2 Proton Channel. *PNAS*, 111(26):9396–9401, 2014.

[15] L. C. Watkins, R. Liang, J. M. J. Swanson, W. F. DeGrado, and G. A. Voth. Proton-Induced Conformational and Hydration Dynamics in the Influenza A M2 Channel. *JACS*, 141(29):11667–11676, 2019. PMID: 31264413.

[16] L. C. Watkins, W. F. DeGrado, and G. A. Voth. Influenza A M2 Inhibitor Binding Understood through Mechanisms of Excess Proton Stabilization and Channel Dynamics. *JACS*, 142(41):17425–17433, 2020. PMID: 32933245.

[17] L. C. Watkins, W. F. DeGrado, and G. A. Voth. Multiscale Simulation of an Influenza A M2 Channel Mutant Reveals Key Features of Its Markedly Different Proton Transport Behavior. *JACS*, 144(2):769–776, 2022. PMID: 34985907.

[18] F. Joerg, M. Wieder, and C. Schröder. Protex—A Python Utility for Proton Exchange in Molecular Dynamics Simulations. *Front. Chem.*, 11:1140896, 2023.

[19] P. Eastman, J. Swails, J. D. Chodera, R. T. McGibbon, Y. Zhao, K. A. Beauchamp, L. Wang, A. C. Simmonett, M. P. Harrigan, C. D. Stern, R. P. Wiewiora, B. R. Brooks, and V. S. Pande. OpenMM 7: Rapid Development of High Performance Algorithms for Molecular Dynamics. *PLOS Comput. Biol.*, 13(7):e1005659, 2017.

[20] A. D. Geragotelis, M. L. Wood, H. Göddeke, L. Hong, P. D. Webster, E. K. Wong, J. A. Freites, F. Tombola, and D. J. Tobias. Voltage-dependent Structural Models of the Human Hv1 Proton Channel from Long-Timescale Molecular Dynamics Simulations. *PNAS*, 117(24):13490–13498, 2020.

[21] C. Jardin, N. Ohlwein, A. Franzen, G. Chaves, and B. Musset. The pH-dependent Gating of the Human Voltage-gated Proton Channel from Computational Simulations. *Phys. Chem. Chem. Phys.*, 24(17):9964–9977, 2022.

[22] W. Smith. Elements of Molecular Dynamics, 2014.

[23] M. Karplus and J. A. McCammon. Molecular Dynamics Simulations of Biomolecules. *Nat. Struct.Biol.*, 9(9):646–652, 2002.

[24] A.R. Leach. *Molecular Modelling: Principles and Applications*. Pearson education. Longman, 1996.

[25] B. R. Brooks, R. E. Bruccoleri, B. D. Olafson, D. J. States, S. Swaminathan, and M. Karplus. A Program for Macromolecular Energy, Minimization, and Dynamics Calculations. *J. Comput. Chem.*, 4(2):187–217, 1983.

[26] A. D. MacKerell, B. Brooks, C. L. Brooks, L. Nilsson, B. Roux, Y. Won, and M. Karplus. The Energy Function and Its Parameterization, 1998.

[27] B. R. Brooks, C. L. Brooks, A. D. Mackerell, L. Nilsson, R. J. Petrella, B. Roux, Y. Won, G. Archontis, C. Bartels, S. Boresch, A. Caflisch, L. Caves, Q. Cui, A. R. Dinner, M. Feig, S. Fischer, J. Gao, M. Hodoscek, W. Im, K. Kuczera, T. Lazaridis, J. Ma, V. Ovchinnikov, E. Paci, R. W. Pastor, C. B. Post, J. Z. Pu, M. Schaefer, B. Tidor, R. M. Venable, H. L. Woodcock, X. Wu, W. Yang, D. M. York, and M. Karplus. CHARMM: The Biomolecular Simulation Program. *J. Comput. Chem.*, 30(10):1545–1614, 2009.

[28] E. Hairer, S.P. Nørsett, and G. Wanner. *Solving Ordinary Differential Equations I: Nonstiff Problems*. Springer Series in Computational Mathematics. Springer Berlin Heidelberg, 2008.

[29] L. Verlet. Computer "Experiments" on Classical Fluids. I. Thermodynamical Properties of Lennard-Jones Molecules. *Phys. Rev.*, 159(1):98–103, 1967.

[30] P. H. Hünenberger. Thermostat Algorithms for Molecular Dynamics Simulations. *Adv. Polym. Sci.*, 173:105–147, 2005.

[31] M.P. Allen and D.J. Tildesley. *Computer Simulation of Liquids*. Computer Simulation of Liquids. Clarendon Press, 1989.

[32] Q. Spreiter and M. Walter. Classical Molecular Dynamics Simulation with the Velocity Verlet Algorithm at Strong External Magnetic Fields. *J. Comp. Phys.*, 152(1):102–119, 1999.

[33] C. M. Breneman and K. B. Wiberg. Determining Atom-Centered Monopoles from Molecular Electrostatic Potentials. The Need for High Sampling Density in Formamide Conformational Analysis. *J. Comput. Chem.*, 11(3):361–373, 1990.

[34] R.J Woods and R Chappelle. Restrained Electrostatic Potential Atomic Partial Charges for Condensed-phase Simulations of Carbohydrates. *Theochem.*, 527(1–3):149–156, 2000.

[35] M. E. Tuckerman and G. J. Martyna. Understanding Modern Molecular Dynamics: Techniques and Applications. *JPCB*, 104(2):159–178, 2000.

[36] M. Salanne. Simulations of Room Temperature Ionic Liquids: From Polarizable to Coarse-grained Force Fields. *PCCP*, 17(22):14270–14279, 2015.

[37] D. Bedrov, J. Piquemal, O. Borodin, A. D. MacKerell, B. Roux, and C. Schröder. Molecular Dynamics Simulations of Ionic Liquids and Electrolytes Using Polarizable Force Fields. *Chem. Rev.*, 119(13):7940–7995, 2019.

[38] C. R. Mann. The Theory of Optics. *Science*, 18(457):432–434, 1903.

[39] A. Kumar, O. Yoluk, and A. D. MacKerell. FFParam: Standalone Package for CHARMM Additive and Drude Polarizable Force Field Parametrization of Small Molecules. *J. Comput. Chem.*, 41(9):958–970, 2019.

[40] F. Lin, J. Huang, P. Pandey, C. Rupakheti, J. Li, B. Roux, and A. D. MacKerell. Further Optimization and Validation of the Classical Drude Polarizable Protein Force Field. *J. Chem. Theory Comput.*, 16(5):3221–3239, 2020.

[41] J. Huang, S. Rauscher, G. Nawrocki, T. Ran, M. Feig, B. L. de Groot, H. Grubmüller, and A. D. MacKerell. CHARMM36m: an Improved Force Field for Folded and Intrinsically Disordered Proteins. *Nat. Methods*, 14(1):71–73, 2016.

[42] J. A. Lemkul, J. Huang, B. Roux, and A. D. MacKerell. An Empirical Polarizable Force Field Based on the Classical Drude Oscillator Model: Development History and Recent Applications. *Chem. Rev.*, 116(9):4983–5013, 2016.

[43] T. P Senftle, S. Hong, M. M. Islam, S. B. Kylasa, Y. Zheng, Y. K. Shin, C. Junkermeier, R. Engel-Herbert, M. J. Janik, H. M. Aktulga, T. Verstraelen, A. Grama, and A. C. T. van Duin. The ReaxFF Reactive Force-field: Development, Applications and Future Directions. *npj Comput Mater*, 2:15011, 2016.

[44] K. Farah, F. Müller-Plathe, and M. C. Böhm. Classical Reactive Molecular Dynamics Implementations: State of the Art. *ChemPhysChem*, 13:1127–1151, 2012.

[45] A. S. J. S. Mey, B. K. Allen, H. E. B. McDonald, J. D. Chodera, D. F. Hahn, M. Kuhn, J. Michel, D. L. Mobley, L. N. Naden, S. Prasad, A. Rizzi, J. Scheen, M. R. Shirts, G. Tresadern, and H. Xu. Best Practices for Alchemical Free Energy Calculations. *LiveCoMS*, 2:18378, 2020.

[46] R. Jacobi, F. Joerg, O. Steinhauser, and C. Schröder. Emulating Proton Transfer Reactions in the Pseudo-protic Ionic Liquid 1-Methylimidazolium Acetate. *PCCP*, 24(16):9277–9285, 2022.

[47] D. Chandler. *Introduction to Modern Statistical Mechanics*. Oxford University Press, 1987.

[48] C. Schröder, T. Rudas, G. Neumayr, W. Gansterer, and O. Steinhauser. Impact of Anisotropy on the Structure and Dynamics of Ionic Liquids: A Computational Study of 1-Butyl-3-Methyl-Imidazolium Trifluoroacetate. *J. Chem. Phys.*, 127(4), 2007.

[49] I. Kufareva and R. Abagyan. *Methods of Protein Structure Comparison*, page 231–257. Humana Press, 2011.

[50] A. Fick. Ueber Diffusion. *Annalen der Physik*, 170(1):59–86, 1855.

[51] K. Deshmukh, S. Sankaran, B. Ahamed, K. K. Sadasivuni, K. S.K. Pasha, D. Ponnamma, P.S. Rama Sreekanth, and K. Chidambaram. Chapter 10 - dielectric spectroscopy. In *Spectroscopic Methods for Nanomaterials Characterization*, Micro and Nano Technologies, pages 237–299. Elsevier, 2017.

[52] F. Kremer and A. Schönhals. *Broadband Dielectric Spectroscopy*. Springer Berlin Heidelberg, 2012.

[53] W. H. H. Woodward. *Broadband Dielectric Spectroscopy—A Practical Guide*, page 3–59. ACS, 2021.

[54] C. Schröder and O. Steinhauser. Using Fit Functions in Computational Dielectric Spectroscopy. *J. Chem. Phys.*, 132(24), 2010.

[55] M. Sega and C. Schröder. Dielectric and Terahertz Spectroscopy of Polarizable and Nonpolarizable Water Models: A Comparative Study. *JPCA*, 119(9):1539–1547, 2014.

[56] J. Calais. Density-functional Theory of Atoms and Molecule. *Int. J. Quantum Chem.*, 47(1):101–101, 1989.

[57] Koch, W. and Holthausen, M. C. *Hydrogen Bonds and Weakly Bound Systems*, chapter 12, pages 217–238. John Wiley & Sons, Ltd, 2001.

[58] M. J. Frisch, G. W. Trucks, H. B. Schlegel, G. E. Scuseria, M. A. Robb, J. R. Cheeseman, G. Scalmani, V. Barone, G. A. Petersson, H. Nakatsuji, X. Li, M. Caricato, A. V. Marenich, J. Bloino, B. G. Janesko, R. Gomperts, B. Mennucci, H. P. Hratchian, J. V. Ortiz, A. F. Izmaylov, J. L. Sonnenberg, D. Williams-Young, F. Ding, F. Lipparini, F. Egidi, J. Goings, B. Peng, A. Petrone, T. Henderson, D. Ranasinghe, V. G. Zakrzewski, J. Gao, N. Rega, G. Zheng, W. Liang, M. Hada, M. Ehara, K. Toyota, R. Fukuda, J. Hasegawa, M. Ishida, T. Nakajima, Y. Honda, O. Kitao, H. Nakai, T. Vreven, K. Throssell, J. A. Montgomery, Jr., J. E. Peralta, F. Ogliaro, M. J. Bearpark, J. J. Heyd, E. N. Brothers, K. N. Kudin, V. N. Staroverov, T. A. Keith, R. Kobayashi, J. Normand, K. Raghavachari, A. P. Rendell, J. C. Burant, S. S. Iyengar, J. Tomasi, M. Cossi, J. M. Millam, M. Klene, C. Adamo, R. Cammi, J. W. Ochterski, R. L. Martin, K. Morokuma, O. Farkas, J. B. Foresman, and D. J. Fox. Gaussian˜16 Revision C.01, 2016. Gaussian Inc. Wallingford CT.

[59] D. A. Becke. Density-functional Thermochemistry III. The Role of Exact Exchange. *J. of Chem. Phys.*, pages 5648–5652, 1993.

[60] S. Grimme, A. Hansen, J. G. Brandenburg, and C. Bannwarth. Dispersion-Corrected Mean-Field Electronic Structure Methods. *Chem. Rev.*, 116(9):5105–5154, 2016. PMID: 27077966.

[61] N. Kosar, K. Ayub, M. A. Gilani, S. Muhammad, and T. Mahmood. Benchmark Density Functional Theory Approach for the Calculation of Bond Dissociation

Energies of the M–O2 Bond: A Key Step in Water Splitting Reactions. *ACS Omega*, 7(24):20800–20808, 2022.

[62] T. Clark, J. Chandrasekhar, G. W. Spitznagel, and P. V. R. Schleyer. Efficient Diffuse Function-augmented Basis Sets for Anion Calculations. III. The 3-21+G Basis Set for First-row Elements, Li-F. *J. Comput. Chem.*, 4:294–301, 1983.

[63] R. Krishnan, J. S. Binkley, R. Seeger, and J. A. Pople. Self-consistent Molecular Orbital Methods. XX. A Basis Set for Correlated Wave Functions. *J. Chem. Phys.*, 72:650–654, 1980.

[64] J. Tomasi, B. Mennucci, and R. Cammi. Quantum Mechanical Continuum Solvation Models. *Chem. Rev.*, 105(8):2999–3094, 2005. PMID: 16092826.

[65] B. Mennucci, J. Tomasi, R. Cammi, J. R. Cheeseman, M. J. Frisch, F. J. Devlin, S. Gabriel, and P. J. Stephens. Polarizable Continuum Model (PCM) Calculations of Solvent Effects on Optical Rotations of Chiral Molecules. *JPCA*, 106(25):6102–6113, 2002.

[66] L. Martínez, R. Andrade, E. G. Birgin, and J. M. Martínez. PACKMOL: A Package for Building Initial Configurations for Molecular Dynamics Simulations. *J. Comput. Chem.*, 30(13):2157–2164, 2009.

[67] K. Vanommeslaeghe, E. Hatcher, C. Acharya, S. Kundu, S. Zhong, J. Shim, E. Darian, O. Guvench, P. Lopes, I. Vorobyov, and A. D. Mackerell. CHARMM General Force Field: A Force Field for Drug-like Molecules Compatible with the CHARMM All-atom Additive Biological Force Fields. *J. Comput. Chem.*, 31(4):671–690, 2009.

[68] J. Ryckaert, G. Ciccotti, and H. J.C Berendsen. Numerical Integration of the Cartesian Equations of Motion of a System with Constraints: Molecular Dynamics of n-Alkanes. *J. Comp. Phys.*, 23(3):327–341, 1977.

[69] T. Darden, D. York, and L. Pedersen. Particle mesh Ewald: An $N \cdot \log(N)$ Method for Ewald Sums in Large Systems. *J. Chem. Phys.*, 98(12):10089–10092, 1993.

[70] U. Essmann, L. Perera, M. L. Berkowitz, T. Darden, H. Lee, and L. G. Pedersen. A Smooth Particle Mesh Ewald Method. *J. Chem. Phys.*, 103(19):8577–8593, 1995.

[71] https://github.com/z-gong/openmm-velocityVerlet.

[72] S. Jo, T. Kim, V. G. Iyer, and W. Im. CHARMM-GUI: A Web-based Graphical User Interface for CHARMM. *J. Comput. Chem.*, 29(11):1859–1865, 2008.

[73] J. Lee, X. Cheng, J. M. Swails, M. Yeom, P. K. Eastman, J. A. Lemkul, S. Wei, J. Buckner, J. Jeong, Y. Qi, S. Jo, V. S. Pande, D. A. Case, C. L. Brooks, A. D. Jr. MacKerell, J. B. Klauda, and W. Im. CHARMM-GUI Input Generator for NAMD, GROMACS, AMBER, OpenMM, and CHARMM/OpenMM Simulations Using the

CHARMM36 Additive Force Field. *J. Chem. Theory Comput.*, 12(1):405–413, 2016. PMID: 26631602.

[74] S. Jo, T. Kim, and W. Im. Automated Builder and Database of Protein/Membrane Complexes for Molecular Dynamics Simulations. *PLoS ONE*, 2(9):e880, 2007.

[75] E. L. Wu, X.Cheng, S. Jo, H. Rui, K. C. Song, E. M. Dávila-Contreras, Y. Qi, J. Lee, V. Monje-Galvan, R. M. Venable, J. B. Klauda, and W. Im. CHARMM-GUI Membrane Builder Toward Realistic Biological Membrane Simulations. *J. Comput. Chem.*, 35(27):1997–2004, 2014.

[76] K. Nishimura, S. Kim, L. Zhang, and T.A. Cross. The Closed State Structure of M2 Protein H^+ Channel by Solid State NMR Spectroscopy, 2003.

[77] R. Acharya, A.L. Polishchuk, and W.F. DeGrado. High Resolution Crystal Structure of Transmembrane Domain of M2, 2010.

[78] M. Sharma, M. Yi, H. Dong, H. Qin, E. Peterson, D.D. Busath, H.X. Zhou, and T.A. Cross. Solid State NMR Structure of the M2 Proton Channel from Influenza A Virus in Hydrated Lipid Bilayer, 2010.

[79] I. Kass and Isaiah T. A. How pH Open a H^+ Channel: The Gating Mechanism of Influenza A M2. *Structure*, 13:1789–1798, 2005.

[80] Y. Gao, J. Lee, I. P. S. Smith, H. Lee, S. Kim, Y. Qi, J. B. Klauda, G. Widmalm, S. Khalid, and W. Im. CHARMM-GUI Supports Hydrogen Mass Repartitioning and Different Protonation States of Phosphates in Lipopolysaccharides. *J. Chem. Inf. Model.*, 61(2):831–839, 2021. PMID: 33442985.

[81] S. Jo, J. B. Lim, J. B. Klauda, and W. Im. CHARMM-GUI Membrane Builder for Mixed Bilayers and Its Application to Yeast Membranes. *Biophys. J.*, 97(1):50–58, 2009.

[82] J. Lee, D. S. Patel, J. Ståhle, S. Park, N. R. Kern, S. Kim, J. Lee, X. Cheng, M. A. Valvano, O. Holst, Y. A. Knirel, Y. Qi, S. Jo, J. B. Klauda, G. Widmalm, and W. Im. CHARMM-GUI Membrane Builder for Complex Biological Membrane Simulations with Glycolipids and Lipoglycans. *J. Chem. Theory Comput.*, 15(1):775–786, 2018.

[83] G. Lamoureux, E. Harder, I. V. Vorobyov, B. Roux, and A. D. MacKerell. A Polarizable Model of Water for Molecular Dynamics Simulations of Biomolecules. *Chem. Phys. Lett.*, 418(1–3):245–249, 2006.

[84] C. M. Baker, V. M. Anisimov, and A. D. MacKerell. Development of CHARMM Polarizable Force Field for Nucleic Acid Bases Based on the Classical Drude Oscillator Model. *J. Phys. Chem. B*, 115(3):580–596, 2010.

[85] P. E. M. Lopes, J. Huang, J. Shim, Y. Luo, H. Li, Be. Roux, and A. D. MacKerell. Polarizable Force Field for Peptides and Proteins Based on the Classical Drude Oscillator. *J. Chem. Theory Comput.*, 9(12):5430–5449, 2013.

[86] N. Michaud-Agrawal, E. J. Denning, T. B. Woolf, and O. Beckstein. MDAnalysis: A Toolkit for the Analysis of Molecular Dynamics Simulations. *J. Comput. Chem.*, 32(10):2319–2327, April 2011.

[87] R. Gowers, M. Linke, J. Barnoud, T. Reddy, M. Melo, S. Seyler, J. Domański, D. Dotson, S. Buchoux, I. Kenney, and O. Beckstein. MDAnalysis: A Python Package for the Rapid Analysis of Molecular Dynamics Simulations. In *Proceedings of the 15th Python in Science Conference*, SciPy. SciPy, 2016.

[88] C. Schröder and O. Steinhauser. Using Fit Functions in Computational Dielectric Spectroscopy. *J. Chem. Phys.*, 132(24):244109, 2010.

[89] M. Petřek, P. Košinová, J. Koča, and M. Otyepka. MOLE: A Voronoi Diagram-Based Explorer of Molecular Channels, Pores, and Tunnels. *Structure*, 15(11):1357–1363, 2007.

[90] D. Sehnal, R. Svobodová Vařeková, K. Berka, L. Pravda, V. Navrátilová, P. Banáš, C. Ionescu, M. Otyepka, and J. Koča. MOLE 2.0: Advanced Approach for Analysis of Biomacromolecular Channels. *J. Cheminform*, 5(1), 2013.

[91] https://mole.upol.cz/online/.

[92] M. Schröder, F. Gatti, D. Lauvergnat, H. Meyer, and O. Vendrell. The Coupling of the Hydrated Proton to Its First Solvation Shell. *Nat. Commun.*, 13(1), 2022.

[93] J. Kolafa. A Polarizable Three-Site Water Model with Intramolecular Polarizability. *Collect. Czechoslov. Chem. Commun.*, 73(4):507–517, 2008.

[94] M. Tanaka, G. Girard, R. Davis, A. Peuto, and N. Bignell. Recommended Table for the Density of Water Between 0^{circ}C and 40^{circ}C Based on Recent Experimental Reports. *Metrologia*, 38(4):301–309, 2001.

[95] K. R. Harris and L. A. Woolf. Pressure and Temperature Dependence of the Self Diffusion Coefficient of Water and Oxygen-18 Water. *J. Chem. Soc., Faraday Trans. 1*, 76:377–385, 1980.

[96] Johannes Fiedler, Mathias Boström, Clas Persson, Iver Brevik, Robert Corkery, Stefan Yoshi Buhmann, and Drew F. Parsons. Full-Spectrum High-Resolution Modeling of the Dielectric Function of Water. *JPCB*, 124(15):3103–3113, 2020. PMID: 32208624.

[97] D. D. Kemp and M. S. Gordon. An Interpretation of the Enhancement of the Water Dipole Moment Due to the Presence of Other Water Molecules. *JPCA*, 112(22):4885–4894, 2008.

[98] S. Pinon, D. L. Diedhiou, A-M. Gue, N. Fabre, G. Prigent, V. Conedera, E. Rius, C. Quendo, B. Potelon, J-F. Favennec, and A. Boukabache. Development of a Microsystem Based on a Microfluidic Network to Tune and Reconfigure RF Circuits. *JMM*, 22(7):074005, 2012.

[99] S. Phongphanphanee, T. Rungrotmongkol, N. Yoshida, S. Hannongbua, and F. Hirata. Proton Transport through the Influenza A M2 Channel: Three-Dimensional Reference Interaction Site Model Study. *JACS*, 132(28):9782–9788, 2010. PMID: 20578761.

[100] P. Intharathep, C. Laohpongspaisan, T. Rungrotmongkol, A. Loisruangsin, M. Malaisree, P. Decha, O. Aruksakunwong, K. Chuenpennit, N. Kaiyawet, P. Sompornpisut, S. Pianwanit, and S. Hannongbua. How Amantadine and Rimantadine Inhibit Proton Transport in the M2 Protein Channel. *J. Mol. Graph. Model.*, 27(3):342–348, 2008.

[101] P. Intharathep, T. Rungrotmongkol, P. Decha, N. Nunthaboot, N. Kaiyawet, T. Kerdcharoen, P. Sompornpisut, and S. Hannongbua. Evaluating How Rimantadines Control the Proton Gating of the Influenza A M2-proton Port via Allosteric Binding Outside of the M2-channel: MD Simulations. *J. Enzyme Inhib. Med. Chem.*, 26(2):162–168, 2011. PMID: 20583869.

[102] L. R. Forrest, A. Kukol, I. T. Arkin, D. P. Tieleman, and M. S.P. Sansom. Exploring Models of the Influenza A M2 Channel: MD Simulations in a Phospholipid Bilayer. *Biophys. J.*, 78(1):55–69, 2000.

[103] M. A. Wilson, C. Wei, P. Bjelkmar, B.A. Wallace, and A. Pohorille. Molecular Dynamics Simulation of the Antiamoebin Ion Channel: Linking Structure and Conductance. *Biophys. J.*, 100(10):2394–2402, 2011.

[104] T. Rungrotmongkol, P. Yotmanee, N. Nunthaboot, and S. Hannongbua. Computational Studies of Influenza A Virus at Three Important Targets: Hemagglutinin, Neuraminidase and M2 Protein. *Curr. Pharm. Des.*, 17(17):1720–1739, 2011.